Influence of Cloud Retrieval Errors Due to Three Dimensional Radiative Effects on Calculations of Broadband Shortwave Cloud Radiative Effect

Adeleke S. Ademakinwa[1,2], Zahid H. Tushar[3], Jianyu Zheng[1,2], Chenxi Wang[2,4], Sanjay Purushotham[3], Jianwu Wang[3], Kerry G. Meyer[4], Tamas Várnai[2,4], Zhibo Zhang[1,2,*]

1. Physics Department, University of Maryland Baltimore County (UMBC)
2. Goddard Earth Sciences Technology and Research (GESTAR) II, UMBC
3. Department of Information Systems, UMBC
4. Climate and Radiation Laboratory Code 613, NASA Godard Space Flight Center

*Corresponding author: Zhibo Zhang, zhibo.zhang@umbc.edu

Abstract

12   We investigate how cloud retrieval errors due to the three-dimensional (3D) radiative effects affect
13   broadband shortwave (SW) cloud radiative effects (CRE) in shallow cumulus clouds. A framework based
14   on the combination of large eddy simulations (LES) and radiative transfer (RT) models was developed to
15   simulate both one-dimensional (1D) and 3D radiance, and SW broadband fluxes. Results show that the
16   broadband SW fluxes reflected at top-of-the-domain, transmitted at the surface, and absorbed in the
17   atmosphere, computed from the cloud retrievals using 1D RT (F_{1D}^*) can provide reasonable broadband
18   radiative energy estimates in comparison with those derived from the true cloud fields using 1D RT (F_{1D}).
19   The difference between these 1D RT simulated fluxes (F_{1D}^*, F_{1D}) and the benchmark 3D RT simulations
20   computed from the true cloud field (F_{3D}), depends primarily on the horizontal transport of photons in 3D
21   RT, whose characteristics vary with the sun's geometry. When the solar zenith angle (SZA) is 5°, the
22   domain-averaged F_{1D}^* are in excellent agreement with the F_{3D}, all within 7% relative CRE bias. When the
23   SZA is 60°, the CRE differences between calculations from F_{1D}^* and F_{3D} are determined by how the cloud
24   side-brightening and darkening effects offset each other in the radiance, retrieval, and broadband fluxes.
25   This study suggests that although the cloud property retrievals based on the 1D RT theory may be biased
26   due to the 3D radiative effects, they still provide CRE estimates that are comparable to or better than CRE
27   calculated from the true cloud properties using 1D RT.

1. Introduction

Covering about 60-70% of the Earth's surface [Rossow and Schiffer, 1999; Vardavas and Taylor, 2011], clouds play a very important role in the Earth's climate system. Clouds can cool the Earth by reflecting shortwave (SW) solar radiative flux back to space and at the same time warm the Earth by retaining the outgoing longwave (LW) infrared radiative flux at the top of the atmosphere (TOA), known as the cloud radiative effects (CRE). The annual global average TOA CRE is approximately $-50\,\mathrm{Wm}^{-2}$ at SW and $30\,\mathrm{Wm}^{-2}$ at LW, resulting in a net CRE of about $-20\,\mathrm{Wm}^{-2}$ [Stocker, 2013]. These strong CRE show that clouds greatly affect the Earth's energy budget [Ramanathan et al., 1989; Kiehl and Trenberth, 1997; Trenberth et al., 2009]. The CRE of clouds is largely determined by the optical and microphysical properties of clouds including the cloud optical thickness (τ), cloud droplet effective radius (r_e), and cloud liquid water path (LWP). Thus, continuous measurements of these cloud properties from regional to global scales are critical to better understand the role of clouds in the climate systems. Currently, satellite based remote sensing is the only way to make such observations. Remotely "retrieved" cloud properties based on these satellite observations are often used to derive the radiative effects of clouds [e.g., Wielicki et al., 1996; Platnick et al., 2003; Loeb and Manalo-Smith, 2005; Oreopoulos et al., 2016] and evaluate the simulations of Earth System Models (ESMs) [Kay et al., 2012; Nam et al., 2012; Song et al., 2018].

A commonly used retrieval technique in passive satellite remote sensing is the bi-spectral retrieval method first developed by Nakajima and King [1990]. It retrieves τ and r_e simultaneously from a pair of total reflectance measurements, one from the non-absorbing visible or near infrared (VNIR) band (e.g., 0.66 µm) and the other from the moderately absorbing short-wave infrared (SWIR) band (e.g., 2.13 µm). Since clouds in reality have three-dimensional (3D) structures, the simulation of radiative transfer (RT) in clouds should ideally consider the transport of radiation in both vertical and horizontal directions (referred to as "3D RT"). Unfortunately, the computational cost for 3D RT is extremely high. As a result, the operational bi-spectral cloud retrievals are almost exclusively based on the one-dimensional (1D) RT theory that considers only the vertical and ignores the net horizontal transport of radiation. The radiative properties of clouds under 3D RT are substantially different from those under 1D RT. This is known as the 3D radiative effects and can lead to substantial biases in the cloud property retrievals based on 1D RT [Várnai et al., 2001; Marshak et al., 2006; Zhang et al. 2012; Zhang et al. 2016]. Although recent efforts have been made to employ machine learning techniques to retrieve cloud properties based on 3D RT theory [Okamura et al., 2017; Masuda et al., 2019; Nataraja et al., 2022], these machine-learning based algorithms are still in their infancy and far from being used in operational algorithms.

Many previous studies have investigated the 3D radiative effects on satellite radiance observations and cloud property retrievals. For example, Welch and Wielicki [1984] used some "toy" cloud fields (e.g., cubic, and cylindrical) to illustrate the impact of side-illuminating and mutual shadowing on cloud albedo. Várnai and Davis [1999] and Várnai [2000] elucidated several 3D RT mechanisms, e.g., upward/downward trapping/escaping, that can result in significant differences between 1D and 3D cloud albedo. Hogan et al. [2019] proposed a distinct mechanism, named "entrapment" which play a key role in the 3D radiative effect of clouds. Davis and Marshak [2001] pointed out that the channeling effect in 3D RT can smoothen out the small-scale cloud variations and lead to the reduction of cloud brightness at cloud edges. Marshak et al. [2006] explained how the radiance biases due to 3D radiative effects can lead to τ and r_e retrieval biases in MODIS (Moderate Resolution Imaging Spectroradiometer) cloud products. This study is built upon these classic papers but has a different objective.

70   Here, we investigate an important question: Do cloud property retrievals based on 1D RT, which
71   are potentially biased due to the 3D radiative effects, still provide an observational basis to estimate the
72   broadband SW CRE? This is an important question because as mentioned above, operational cloud
73   retrieval products from, for example MODIS, are frequently used for CRE estimation and ESM evaluation.
74   However, to our best knowledge, the impacts of retrieval bias due to the 3D radiative effects on such
75   applications have never been examined systematically in previous studies. To better explain our objective
76   and the difference of this study from many previous ones on the 3D radiative effects, we need to introduce
77   a framework illustrated in **Fig. 1**. As conceptually illustrated in **Fig. 1**, the observed radiances are inherently
78   3D (i.e., from Box A to C) because the RT in nature is 3D. However, when 1D RT theory is used to interpret
79   the observations, we get the "retrieved cloud properties" in Box D that can be significantly different from
80   the "true" cloud properties in Box A. Although the retrieved cloud properties are often biased due to the
81   3D radiative effects, they are still widely used to compute the radiative fluxes by clouds (i.e., from Box D
82   to E) using 1D RT and the results are often used for studying the climatic effects of clouds [e.g., Kato et al.,
83   2011; Zelinka et al., 2012; Oreopoulos et al., 2016]. In contrast, the "true" radiative fluxes in nature are
84   also 3D (i.e., from Box A to F). A few recent studies have computed and compared the 1D and 3D radiative
85   fluxes and heating rates by clouds. For example, Barker et al. [2011, 2012] and Okata et al. [2017]
86   compared the 1D and 3D SW fluxes computed based on the constructed A-Train cloud scenes at the TOA
87   and surface. A more recent study by Singer et al. [2021] utilized Large-Eddy Simulations (LES) cloud fields
88   of different cloud regimes to assess the SW radiative flux and TOA albedo bias associated with the 3D
89   effects. The main difference between their study and this current work is as follows: They compared the
90   3D (i.e., Box F in **Fig. 1**) with the 1D broadband fluxes (i.e., Box G in **Fig. 1**) both computed from the "true"
91   clouds. In contrast, we argue that the "true" clouds are not known in practice and therefore we compare
92   the 3D flux (i.e., Box F in **Fig. 1**) with the 1D flux computed from the "retrieved cloud properties" (i.e., Box
93   E in **Fig. 1**), this approach enables us to measure the impact of cloud retrieval errors on the radiative flux
94   and CRE.
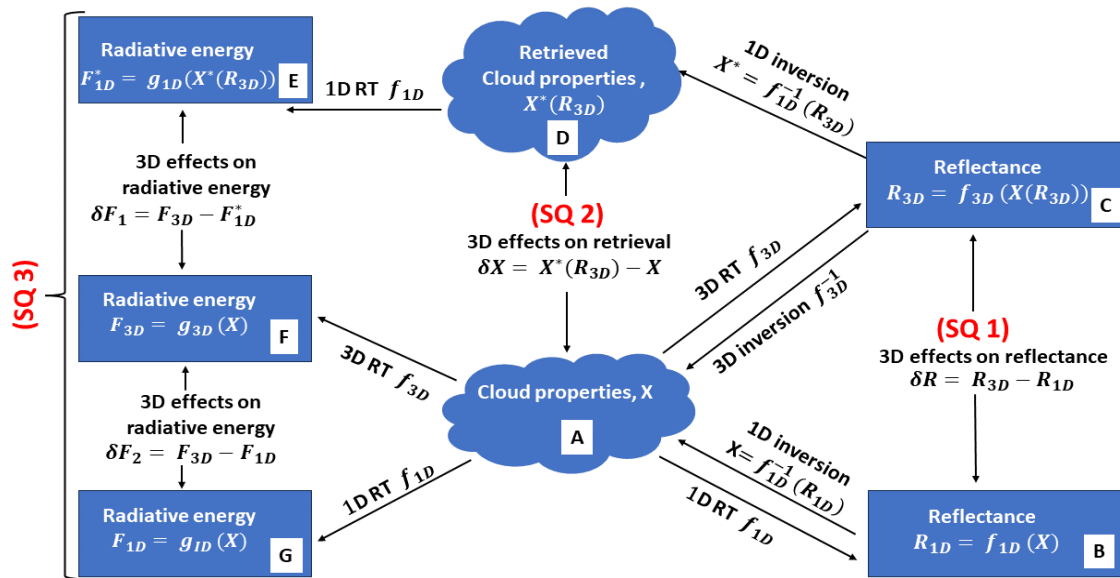
95

96   **Fig. 1.** Conceptual framework to understand the study. R_{3D} and R_{1D} are the reflectance from three dimensional (3D) and one
97   dimensional (1D) radiative transfer (RT) respectively, while δR is their difference. X represent the true cloud field and $X^*(R_{3D})$

98 is the retrieved cloud properties from 3D RT reflectance, while δX is the cloud property retrieval bias. F_{1D}^* and F_{1D} are the
99 radiative flux calculated using 1D RT on the retrieved cloud properties and true cloud properties respectively. F_{3D} is the radiative
100 flux derived from the true cloud field using 3D RT. δF_1 and δF_2 are the difference between the pair (F_{1D}^*, F_{3D}) and (F_{1D}, F_{3D}),
101 respectively.

102 To determine whether biased cloud retrievals of cloud properties can still provide an observational basis
103 for CRE, we focus on three important scientific questions (SQs) as illustrated in **Fig. 1:**

- SQ 1: How does the reflectance simulated based on 3D RT (R_{3D}) compare with the reflectance
  simulated based on 1D RT (R_{1D}) for different types of clouds at different illuminating-viewing
  geometries? (i.e., Comparing Box C to B in **Fig. 1**).
- SQ 2: How does the "retrieved cloud properties", e.g., cloud optical thickness and cloud droplet
  effective radius derived from the 3D reflectance using 1D RT, compare to the "true" cloud
  properties? (i.e., Comparing Box D to A in **Fig. 1**).
- SQ 3: Comparing δF_1 to δF_2 in **Fig. 1**: i.e., how are the broadband SW radiative fluxes derived
  from the retrieved cloud properties using 1D RT, F_{1D}^* (see Box E in **Fig. 1**) different from the "true"
  radiative fluxes computed from the "true" cloud fields using 3D RT, F_{3D} (see Box F in **Fig. 1**) ? And
  how does this result compare with the difference between F_{3D} and the broadband SW radiative
  fluxes computed from the "true" cloud properties using 1D RT, F_{1D} (see Box G in **Fig. 1**).

115 The paper's remaining structure is arranged as follows: Section 2 briefly describes the data and theory for
116 the study. Section 3 presents and discusses results on how the 3D radiative effects influences the radiance
117 fields, cloud property retrievals and broadband radiative flux. The summary and conclusion are given in
118 Sect. 4.

2. Data and Theory
2.1. Cloud field data set

121   A great challenge facing 3D radiative effects studies is that the "true" clouds are always obscured by
122 the 3D radiative effects which are inevitable in real observations. To overcome this challenge, many
123 previous studies [e.g., Zhang et al., 2012; Miller et al., 2018; Rajapakshe and Zhang, 2020] have used
124 synthetic cloud fields and RT simulations to mimic the observation-retrieval process and study the 3D
125 radiative effects. Building on these previous studies, we adopt the same state-of-the-art satellite retrieval
126 simulator by Zhang et al. [2012] and added a broadband flux computation function to study the 3D
127 radiative effects and its impact on broadband SW radiative flux. As described in Zhang et al. [2012] and
128 illustrated in **Fig. 1**, the framework consists of three major components: 1) Synthetic cloud fields; 2) RT
129 models (for radiance and broadband flux simulations); 3) cloud property (e.g., τ and r_e) retrieval
130 simulator. LES cloud fields which are commonly used in different cloud microphysical and 3D effects studies
131 [e.g., Singer at al., 2020, Zhang et al., 2012] are based on computational models and mathematical
132 equations to simulate the atmospheric behavior and get the 3D cloud property, certain studies [e.g., Levis
133 et al., 2015; Loveridge et al., 2023] have developed atmospheric tomography techniques to reconstruct 3D
134 cloud scenes from observational data but are yet to be widely used globally. Similar to Zhang et al. [2012],
135 the synthetic cloud fields utilized in this study are based on LES cloud fields.

136   Since the 3D radiative effects on overcast clouds are minimal, two cloud fields of low and
137 intermediate cloud fractions have been selected as a case study to illustrate the framework explained in
138 Sect. 1. The selected cloud fields were from the LES Atmospheric Radiation Measurement (ARM)

139 Symbiotic Simulation and Observation (LASSO) Activity, conducted in the ARM Southern Great Plain (SGP)
140 site located in Lamont, Oklahoma [Gustafson et al., 2020]
141 (https://www.arm.gov/capabilities/modeling/lasso/). LASSO enhances ARM's observations by using LES
142 modeling to provide contextual and self-consistent representation of the atmosphere surrounding the
143 ARM site. It also provides continuous observations from ground-based cloud and radiometric instruments
144 which is valuable for enhancing research on cloud-radiation interactions. For this study, the two snapshots
145 of LASSO LES cloud field cases analyzed are: 14:00 UTC on 27 June 2015, simulation ID=108 [ARM user
146 facility, 2015] and the other at 14:00 UTC on 18 August 2016, simulation ID=113 [ARM user facility, 2016].
147 For conciseness in this text, these snapshots will be referred to as "27 June" and "18 August" respectively.
148 We chose to use these specific LASSO LES cloud fields data from the stated dates, because it represents
149 typical shallow cumulus clouds, does not contain ice (to avoid the complexities dealing with ice
150 microphysics) and has better diagnostic statistics compared to other LES data streams. It is important to
151 note that, because the impact of 3D radiative effects vary substantially for different cloud regimes and
152 surface types, this study is constrained to shallow cumulus cloud types (over land surface) found in the
153 LASSO SGP site.

154
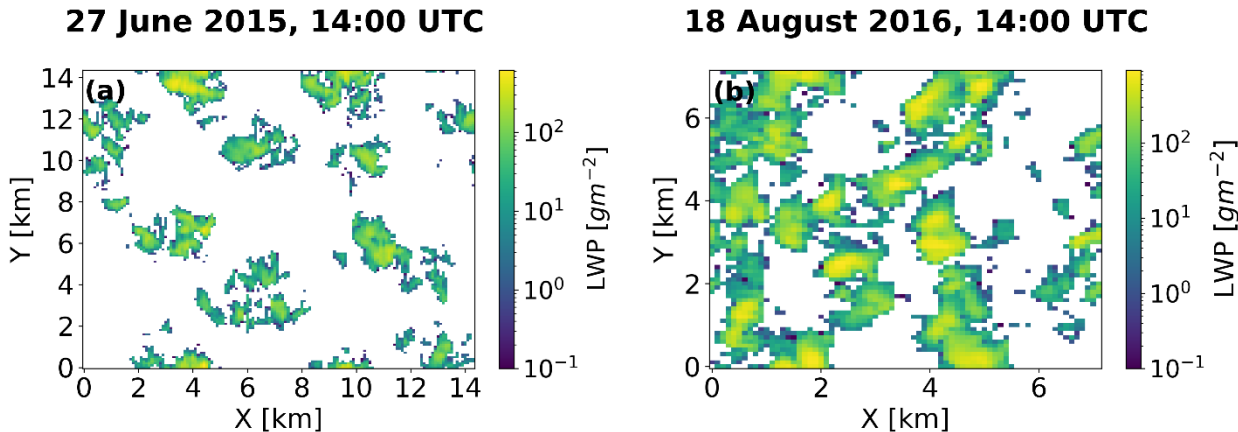
156 **Fig. 2.** Large-Eddy Simulation **(**LES) of cloud liquid water path (LWP) for 14:00 UTC, 27 June 2015 (a), and 14:00 UTC, 18 August
157 2016 (b) at the ARM SGP atmospheric observatory. White areas are clear-sky regions where cloud liquid water path (LWP) =0.

158 The LASSO LES cloud fields for this study are characterized by broken cloud patterns spatially
159 distributed across the domain as seen in the LWP maps in **Fig. 2a and b** for the 27 June and 18 August
160 cases, respectively. The 3D distribution of cloud liquid water content (LWC) was obtained from the LASSO
161 cloud fields data and a two-moment bulk microphysics scheme by Morrison and Gettelman [2008] (see
162 their equation 5 in Sect. 2) was used to obtain the r_e associated with the corresponding LWC distribution.
163 It is important to note that for this study, a cloudy column has been defined as a column with LWP > 0
164 (i.e., clear-sky regions have LWP=0). The cloud fields have different domain sizes and microphysics
165 distribution, and the cloud cover for the 18 August cloud field (47.08%) is more than twice that of the 27
166 June cloud field (20.15%). Information about the cloud properties and the LES domain are summarized in
167 **Table 1**.

168 **Table 1.** Cloud property characteristics for the LES cloud field cases. The mean cloud effective radius (r_e), mean cloud optical
169 thickness (τ)**,** and In-cloud liquid water path are from the average of the cloudy regions only. The columns from left to right are

170 case name, cloud fraction, mean In-cloud liquid water path, mean cloud base height (CBH), mean cloud top height (CTH), mean
171 r_e, mean τ, grid spacing, and domain size, respectively.

Case name	CF (%)	Mean In-cloud LWP ($\mathrm{gm^{-2}}$)	Mean CBH (km)	Mean CTH (km)	Mean r_e (μm)	Mean τ	Grid spacing (m)	Domain size ($\mathrm{km^3}$)
27 June 2015, 14:00 UTC	20.15	51.08	1.979	2.173	7.196	10.95	Δx=Δy=100,Δz=30	14.4x14.4x ~2.8
18 August 2016, 14:00 UTC	47.08	127.67	1.2691	1.6040	8.020	23.24	Δx=Δy=100,Δz=30	7.2 x7.2 x ~2.4

172
173 ## 2.2. Radiative Transfer Setup

174 We use the spherical harmonics discrete ordinate method (SHDOM) RT model developed by Evans
175 [Evans, 1998] to handle both 1D and 3D radiance computations. We have benchmarked the SHDOM
176 simulations against the results from our previous studies [Zhang et al., 2012; Miller et al., 2016].
177 Broadband SW radiative flux computations, both 1D and 3D, were performed with the Intercomparison
178 of 3D Radiation Codes (I3RC) Monte Carlo community model [Pincus and Evans, 2009], and atmospheric
179 gaseous absorption was incorporated via the SW Rapid Radiative Transfer Model (RRTM) correlated
180 k-distribution approach [Mlawer et al., 1997] which consists of 14 bands with spectral range from 0.2 to
181 12 μm (This coupled broadband radiative flux solver is hereafter known as the "I3RC+CKD" model).
182 Rayleigh scattering was included in the flux RT calculations, the background atmospheric profiles are taken
183 to be horizontally homogeneous throughout the domain and the profiles of atmospheric temperature,
184 pressure, ozone, air density and water vapor utilized for the RT flux calculations were obtained from the
185 sounding data at the ARM SGP site on 27 June 2015. Several studies [e.g., Gristey et al., 2022] have shown
186 that aerosol embedded in clouds with small aspect ratios (similar to our chosen LASSO LES cloud fields)
187 have significant influence on the 3D radiative effect. Thus, for simplicity in our study, ambient aerosols
188 are neglected in the RT calculations. The 1D broadband RT flux calculations were performed with the same
189 I3RC+CKD model, by dividing the LES domain into individual columns and RT was calculated on each LES
190 column properties separately and independently.

191 The spectral cloud optical properties were calculated using Mie scattering theory and were
192 averaged over each of the RRTM spectral bands. The phase functions were represented using Legendre
193 coefficients with 35 log spaced effective radius spanning from 2 to 40 μm. The surface was assumed to be
194 Lambertian with surface spectral albedos obtained from the ARM SGP site [see figure 4 in Coddington et
195 al., 2013] applied for wavelength (λ) in the range 0.2 ≤λ≤ 2.5 μm, while surface spectral albedo
196 corresponding to a vegetative covered surface [Zhuravleva et al., 2009] was utilized for λ> 2.5 μm (see
197 Appendix for surface spectral albedo plot used in this study). In the Monte Carlo calculations, 10^8 and 10^4
198 photons were initiated for calculations of the 3D broadband SW flux and the column-independent 1D
199 broadband SW flux, respectively. The radiative transfer calculations were implemented for two solar
200 zenith angles (SZAs), a high sun case with SZA of $5°$ and a low sun case with SZA of $60°$. In the broadband
201 flux calculations, the downward flux at the top of the domain (TOD) corresponds to 1363 $\mathrm{Wm^{-2}}$ and 684.1
202 $\mathrm{Wm^{-2}}$ for SZA $5°$ and $60°$, respectively. Throughout this study, we choose a constant $0°$ solar azimuth

203 angle (SAA) and a constant $0°$ viewing zenith angle (VZA). Double periodic horizontal boundary conditions
204 were applied for all the RT calculations, and all RT calculations have been conducted at the native LES
205 resolution of 100 m. Current satellite remote-sensing instruments have different footprints (e.g., 1 km
206 footprint for MODIS instrument), which can have different 3D effects signatures on the retrievals and
207 impact the derived radiative flux. Therefore, future studies will investigate how 3D effects retrieval errors
208 for different spatial resolutions (coarse and fine) affect the radiative flux estimates.

209   2.3. **Bi-spectral retrieval method**

210 The bi-spectral retrieval method introduced in Sect. 1, is solely based on the 1D RT theory to interpret the
211 observed cloud reflectance. It is implemented using a precomputed Look up table (LUT) which consists of
212 1D reflectance function for different τ and r_e combinations at the required solar-view geometry (an
213 example LUT is shown in **Fig. 3**). The observed cloud reflectance is then utilized as inputs to the LUT to
214 simultaneously retrieve the τ and r_e via a two-dimensional (2D) interpolation between the observed
215 cloud reflectance and the LUT grid. Notably, in the bi-spectral LUT regions with smaller τ, the retrieval
216 uncertainty increases because the isolines of the LUT τ are less orthogonal and more tightly packed.
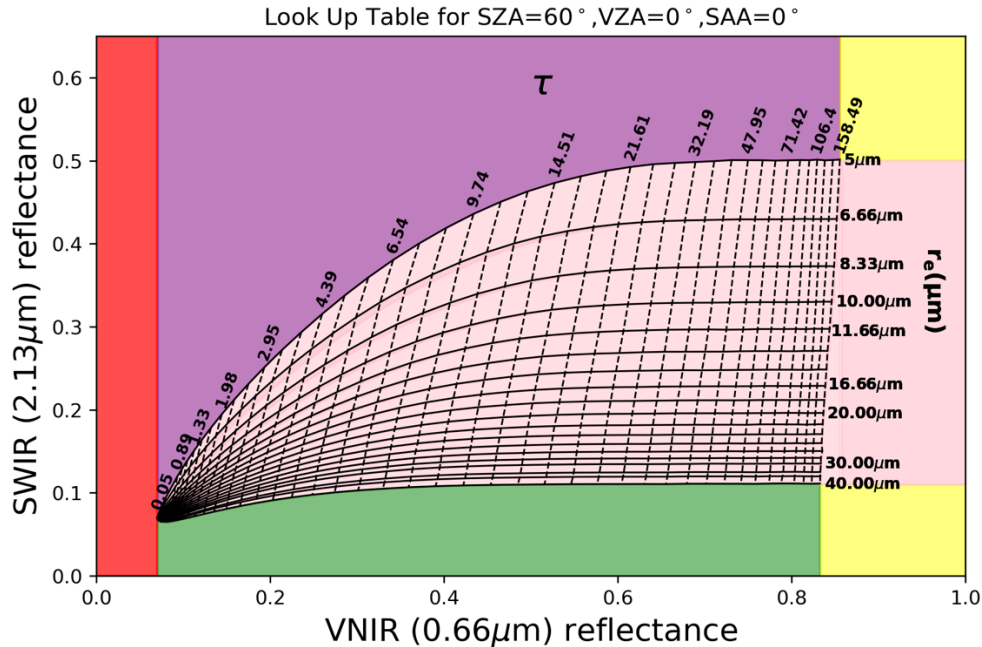
217

218   **Fig. 3.** An example Nakajima and King bi-spectral Look up table (LUT) space. The solid lines are the reflectance function
219   contours for fixed cloud effective radius (r_e), while the dashed lines are for fixed cloud optical thickness (τ). Surface is
220   Lambertian with surface albedo=0.07. The solar zenith angle (SZA) is 60°, the view zenith angle (VZA) is 0°, and the solar
221   azimuth angle (SAA) is 0°.

222 This non-linearity in the LUT has high inhomogeneity consequences for cloud retrievals at the pixel level
223 [Zhang et al., 2012, 2016]. In this study, the VNIR reflectance were measured at 0.66 μm (identical to the
224 central wavelength of operational MODIS retrieval algorithm over a vegetative land surface), while the
225 SWIR reflectance were measured at the 2.13 μm wavelength. The LUT utilized for our bi-spectral retrievals
226 have 19 effective radii spanning from 5 to 40 μm, and 43 log spaced τ values spanning from 0.05 to 158.48.
227 While a constant effective variance (v_e) value of 0.1 is used for consistency with all other RT simulations

228 in this study. The surface albedo in both 0.66 and 2.13 μm wavelengths for the LES radiance simulations
229 and LUT RT calculations was 0.07. This value is consistent with the surface albedo of similar spectral bands
230 in the broadband SW flux computations (see spectral albedo plot in Appendix).

231

232 **2.4. Classification of failed and successful retrievals**

233 One major challenge in cloud property retrievals from satellite remote sensing instruments like
234 MODIS, is the so called "failed retrievals". A retrieval can be considered failed if there is no r_e and τ LUT
235 grid combination to interpret the reflectance observation, or if there is no realistic cloud microphysics to
236 explain the retrieved cloud property (e.g., a retrieved r_e > 40 μm). These can be due to several factors,
237 such as the limits of the LUT, clouds overlapping effect, presence of partially cloudy pixels, extreme solar-
238 satellite viewing geometries, strategy used in cloud mask implementation and the optical characteristics
239 of the underlying surface. Potential causes and rate of occurrence of failed MODIS retrievals for marine
240 liquid phase clouds have been studied extensively [Cho et al., 2015]. In this study, we refer to MODIS cloud
241 property retrieval algorithm's classification of failed retrievals [Platnick et al., 2016] and the study by Cho
242 et al. [2015], to classify a pixel as successful or failed retrieval as explained below:

243 1) For observations with both VNIR and SWIR reflectance observations within the LUT solution
244 space, the nearest interpolated τ and r_e values are retrieved (Pink area bounded by the LUT lines
245 in **Fig. 3**). If the observed VNIR reflectance exceed the upper limit of LUT τ but within the LUT r_e
246 solution range (extended pink area in **Fig. 3**), the nearest LUT r_e is retrieved and the maximum
247 LUT τ value (τ=158.48) is assigned to the retrieval. These explained categories are classified as
248 "successful retrievals" for this study.

249 2) In other cases, for observations with VNIR reflectance within the LUT solution space but SWIR
250 reflectance above the LUT solution space (purple area in **Fig. 3**), the nearest τ values are retrieved
251 but the smallest LUT r_e value of 5 μm is assigned to the retrievals. This category of retrieval failure
252 is called "r_e too small" failures. In cases where the VNIR reflectance observations are within the
253 LUT τ solution space, but the SWIR reflectance are below the LUT solution space (green area in
254 **Fig. 3**) the nearest τ values are retrieved but the largest LUT r_e value of 40 μm is assigned to the
255 retrieval. This category of retrieval failure is called the "r_e too large" failures. In cases where the
256 observed VNIR reflectance is greater than the largest LUT τ value and the observed SWIR
257 reflectance is smaller than the largest LUT r_e (i.e., the lower yellow region in **Fig. 3**), the retrievals
258 are assigned the largest τ value (τ=158.48) and the largest r_e value (r_e=40 μm). For observations
259 with VNIR reflectance greater than the largest LUT τ value and the SWIR reflectance greater than
260 the smallest LUT r_e value (i.e., the upper yellow region in **Fig. 3**), the retrievals are assigned the
261 largest τ value (τ=158.48) and smallest r_e value (r_e=5 μm). Lastly, for observations with VNIR
262 reflectance below the minimum LUT τ (red area in **Fig. 3**), the r_e and τ retrievals are assigned fill
263 values (which are represented by τ = 0 in our flux calculations). These explained categories are
264 called "τ" failures. The r_e too small, r_e too large and τ failure categories are collectively classified
265 as "failed retrievals" for this study.

266

267 **2.5. Approach for radiative transfer simulation and result comparisons**

268 To address the three SQs for our study (identified in Sect. 1), we performed a total of fourteen
269 experiments for each cloud field. The first four experiments were performed with the SHDOM model to

270   study the 3D radiative effects on the observed reflectance and address SQ 1. It involves simulating and
271   comparing R_{3D} with R_{1D} for the high and low sun cases. The next four experiments involve comparing
272   cloud properties retrieved from R_{3D} (Box D in **Fig. 1**) and cloud properties retrieved from R_{1D} (Box B to A
273   in **Fig. 1**) for both high and low sun, to examine the influence of the 3D radiative effects on the retrieved
274   cloud properties and address SQ 2. These experiments were conducted using the 3D and 1D RT based
275   reflectance as inputs to the precomputed LUT described in Sect. 2.3. The last six experiments were
276   conducted with the I3RC+CKD to examine the impact of the 3D radiative effects on the broadband solar
277   radiative flux for both high and low sun scenarios in the LES domains and address SQ 3. These experiments
278   involve calculating for each SZA, F_{1D}^* from the retrieved cloud properties using 1D RT as well as computing
279   F_{3D} and F_{1D} from the true cloud fields using 3D and 1D RT respectively. It is important to note that in the
280   F_{1D}^* calculations, the retrieved cloud properties ($\tau^*(R_{3D})$ and $r_e^*(R_{3D})$) are utilized to calculate the
281   retrieved LWP (using retrieved LWP $\cong 2\tau^*\rho r_e^*/3$, where ρ is the density of liquid water; [Stephens,
282   1977; Liou, 1992]) which are then reconstructed into cloud effective radius and LWC distribution for each
283   LES column while preserving the vertical structure of the original LES cloud field. 1D RT are then performed
284   using the reconstructed retrieved clouds as inputs to obtain F_{1D}^*. Note, unless otherwise stated, for this
285   study, the successful and failed retrievals (as described in Sect. 2.4) have been used to represent the total
286   population of cloudy pixels in the cloud property inputs used to calculate F_{1D}^*. The calculation of F_{1D} is
287   identical to that of F_{3D} except for the absence of the horizontal movement of photons between the LES
288   grid columns. This enables us to determine the impact of neglecting the horizontal movement of photons
289   on the broadband radiative fluxes. On the other hand, in reference to the F_{3D}, computing F_{1D}^* will not
290   only help us to better understand the implications of neglecting the horizontal transport of photons but
291   will also enable us to measure how biases in the retrieved cloud properties (which are affected by the 3D
292   radiative effects) impact the broadband radiative fluxes.

293   In order to describe the impact of the 3D radiative effects on the radiance fields, retrieved cloud
294   properties and broadband radiative flux, we first examine their effects across the LES domain and
295   subsequently quantify their overall impact on the domain by computing the horizontally domain-averaged
296   results and determine the absolute bias, hereafter referred to as "bias" for brevity and is defined as $\bar{y} - \bar{x}$
297   , where $\bar{y}$ denotes the domain-averaged result from the 3D RT quantity (e.g., Reflectance or flux), and $\bar{x}$
298   denotes the domain-averaged result from the 1D RT quantity (e.g., Reflectance or flux).

299   To quantify the difference between the CRE computed from the benchmark F_{3D} and the CRE
300   computed from F_{1D} or F_{1D}^*, we define a domain-scale quantity known as the relative cloud radiative
301   effects (rCRE) bias as:

302
$$\text{rCRE bias} = \left(1 - \frac{\text{CRE}_{1D}}{\text{CRE}_{3D}}\right) \times 100 \tag{1}$$

303   Where CRE_{1D} is the CRE calculated from either F_{1D} or F_{1D}^* in units of Wm^{-2} and CRE_{3D} is the CRE
304   calculated from F_{3D} in units of Wm^{-2}. According to this definition, a rCRE bias of 0% would indicate that
305   there is no bias between the CRE computed from F_{1D} or F_{1D}^* and the CRE computed from F_{3D}. This, imply
306   that the CRE computed from F_{1D} or F_{1D}^* is equivalent to the CRE computed from F_{3D}. A positive rCRE bias
307   greater than 0% would quantify the percentage by which the CRE computed from F_{1D} or F_{1D}^* is lesser than
308   the CRE computed from F_{3D}, and thus indicate that the 1D calculations (F_{1D}, F_{1D}^*) underestimate the CRE
309   relative to F_{3D}. Also, a negative rCRE bias less than 0% would quantify the percentage by which the CRE
310   computed from F_{1D} or F_{1D}^* exceeds the CRE computed from F_{3D} and imply that the calculations from
311   F_{1D} or F_{1D}^* overestimate the CRE relative to F_{3D}.

3. Results and discussion

3.1. Investigating the 3D radiative effects on simulated reflectance

Focusing first on SQ 1, we compare R_{1D} and R_{3D} to assess the impact of the 3D radiative effects on the reflectance radiation field, i.e., Box B vs. Box C in the framework of **Fig. 1**. Specifically, we will investigate the reflectance bias, δR ($\delta R = R_{3D} - R_{1D}$) at the two λ (0.66 and 2.13 μm) required for our bi-spectral retrieval for both low sun (SZA 60°) and high sun (SZA 5°) cases. To describe the 3D radiative effects on the observed reflectance, classifications are made based on the increase in the brightness of a pixel in the LES domain. A pixel in the LES domain is considered "brightened" ("darkened") if its 3D RT-based reflectance is higher (lower) than its 1D counterpart.

Maps of δR at $\lambda = 0.66$ μm ($\delta R_{\lambda=0.66\mu m}$) for the two cloud fields when the sun is high and low are shown in **Fig. 4**. In the low sun case, the deviation of the 1D RT-based simulated reflectance from the 3D RT-based simulated reflectance leads to δR with distinct pattern of brightening and darkening observed in some pixels across the LES domain. A closer examination of $\delta R_{\lambda=0.66\mu m}$ within cloudy regions in the low sun case for the two cloud fields (**Fig. 4b**,**c**) reveals a consistent pattern; the brightened pixels, where $\delta R_{\lambda=0.66\mu m}$ is positive, are predominantly observed in sunlit regions that directly face the sun located on the left (e.g., at X=3.5 km, Y=14 km in **Fig. 4b**). On the other hand, darkened pixels, where $\delta R_{\lambda=0.66\mu m}$ is negative, are observed on the opposite side of the cloud layer (e.g., at X=5 km, Y=14 km in **Fig. 4b**). These findings are consistent with previous 3D radiative effects studies for oblique solar geometry [e.g., Várnai and Davies, 1999; Várnai, 2000; Marshak et al., 2006]. The observed opposing effects of brightening and darkening in the low sun angle case does not only depend on the orientation of the cloud towards or away from the sun, other factors like cloud‑cloud interactions, cloud geometry and aspect ratio, spatial distribution of the cloud in the domain and the horizontal transport of photons also contribute to these behaviors [Várnai and Marshak, 2001, 2002; Marshak and Davis, 2005; Marshak et al., 2006; Zhang et al., 2012].

In the case of the high sun, the sun is almost perpendicular (at SZA 5°), and its radiation interaction with clouds under 3D RT is different from that of the low sun case. In 3D RT at high sun, the original direction of photons is downwards (due to the sun's small angle of inclination to the vertical) and on striking a cloud, some photons are scattered and some leak from optically thick to optically thin cloudy regions and even out of cloud sides [O'Hirok and Gauiter, 1998] down to the surface where they are absorbed. This is because for photons trajectories with low number of scattering trajectories and high sun, photons leaking out of cloud sides are statistically more likely to continue moving downwards towards the surface where they are absorbed. These leaking of photons to surrounding clouds and the surface results in net photon loss in the thick cloud regions, which explains the darkening of the thick clouds and brightening of the surrounding thin clouds compared to 1D RT results. Hence, $\delta R_{\lambda=0.66\mu m}$ is mainly negative across the LES domain for the high sun (**Fig. 4a,c**). The darkening characteristics is more pronounced in the 18 August case because it consists of a larger distribution of thicker clouds compared to the 27 June cloud field; large number of photons leaking from optically thicker clouds results in more significant reduction in the reflectance values and more prominent darkening effect than photons leaking from optically thinner clouds. Similar reflectance characteristics are observed for the 2.13 μm band (not shown).
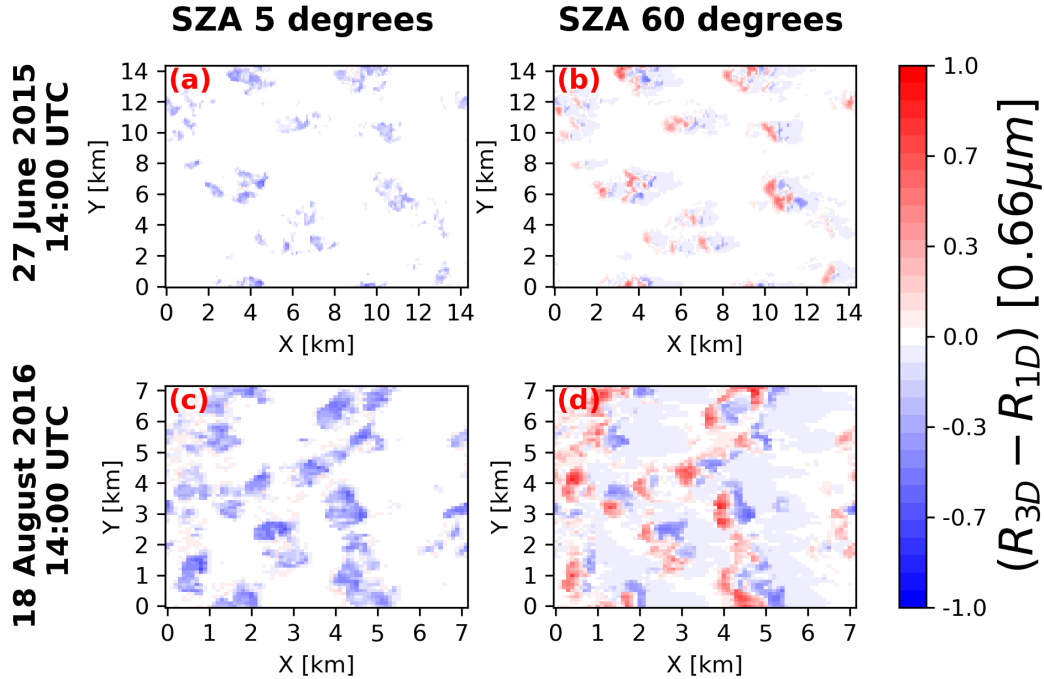
Fig. 4. Maps of the reflectance bias ($\delta R = R_{3D} - R_{1D}$) for wavelength 0.66 μm at Solar zenith angle (SZA) $5°$ (a) and (c) for the 27 June and 18 August cases respectively and SZA $60°$ (b) and (d) for the 27 June and 18 August cases respectively. The direction of view is at nadir. For SZA $5°$, the sun is almost perpendicular to the domain but slightly tilted to the left. For SZA $60°$ the sun is on the left of the domain.

To examine the statistical characteristics of δR in the LES domain, the probability density function (PDF) of δR for "cloudy only" pixels are analyzed to investigate the 3D radiative effects on the observed cloud reflectance. Subsequently, we compared this PDF to δR for both "cloudy and clear-sky" pixels (i.e., the whole LES domain) to highlight the effects of cloud presence on the overall reflectance bias within the LES domain.

The PDFs of δR for cloudy only pixels in the low sun case (broken black and gray lines in **Fig. 5a, b**) are characterized by positive and negative distribution in both VNIR and SWIR bands (corroborating the brightening and darkening effects in Error! Reference source not found.**b,d**). The overall positive δR observed in the VNIR and SWIR bands (domain mean δR of 0.0351 (0.0292) for the VNIR (SWIR) band in the 27 June case and 0.0379 for the VNIR band in the 18 August case) indicates that the brightening effects is predominant when only cloudy pixels are considered. Meanwhile, δR is -0.0233 for the SWIR band in the 18 August case. This negative δR is due to a high net loss of photons in 3D RT reflectance (more photons leak from clouds to the surface where they are absorbed, than those reflected from clouds) compared to the 1D RT results. On the other hand, the PDFs of δR for the cloudy and clear-sky pixels (broken black and gray lines in **Fig. 5c, d**) is almost similar to that of the cloudy only but shows a shift of the distribution leftwards, almost centered around zero. This is expected because clear-sky regions not in the vicinity of any clouds exhibit negligible 3D radiative effects, which causes the distribution to shift closer to zero, since the cloud fraction for both cloud cases is less than 50%. The horizontal movement of photons from cloudy to surrounding clear-sky regions increase the 3D reflectance of clear-sky areas around the sunlit cloudy regions but the strong darkening effects on the clear-sky regions located opposite the sunlit direction dominates the clear-sky only areas, and results in a negative mean bias when the reflectance of

378   clear-sky only pixels are examined. Interestingly, the mean δR for the cloudy and clear-sky pixels are of
379   the same sign with the cloudy only values, which indicates that the cloudy pixels have significant effect on
380   the domain-scale statistics.

381   The PDFs of δR in the case of the high sun for cloudy only pixels show a larger distribution of pixels
382   with positive δR in both the VNIR and SWIR band accompanied by longer tails to the left (red and blue
383   solid lines in **Fig. 5a, b**). However, the δR for both cloud cases present negative values in the VNIR and
384   SWIR bands. These observations suggest that large radiation/photos leak from a small number of thick
385   cloud pixels to a larger number of thin clouds. This phenomenon therefore increases the number of
386   thin clouds with positive reflectance bias, although of very small magnitude when compared to the
387   negative biases.

388
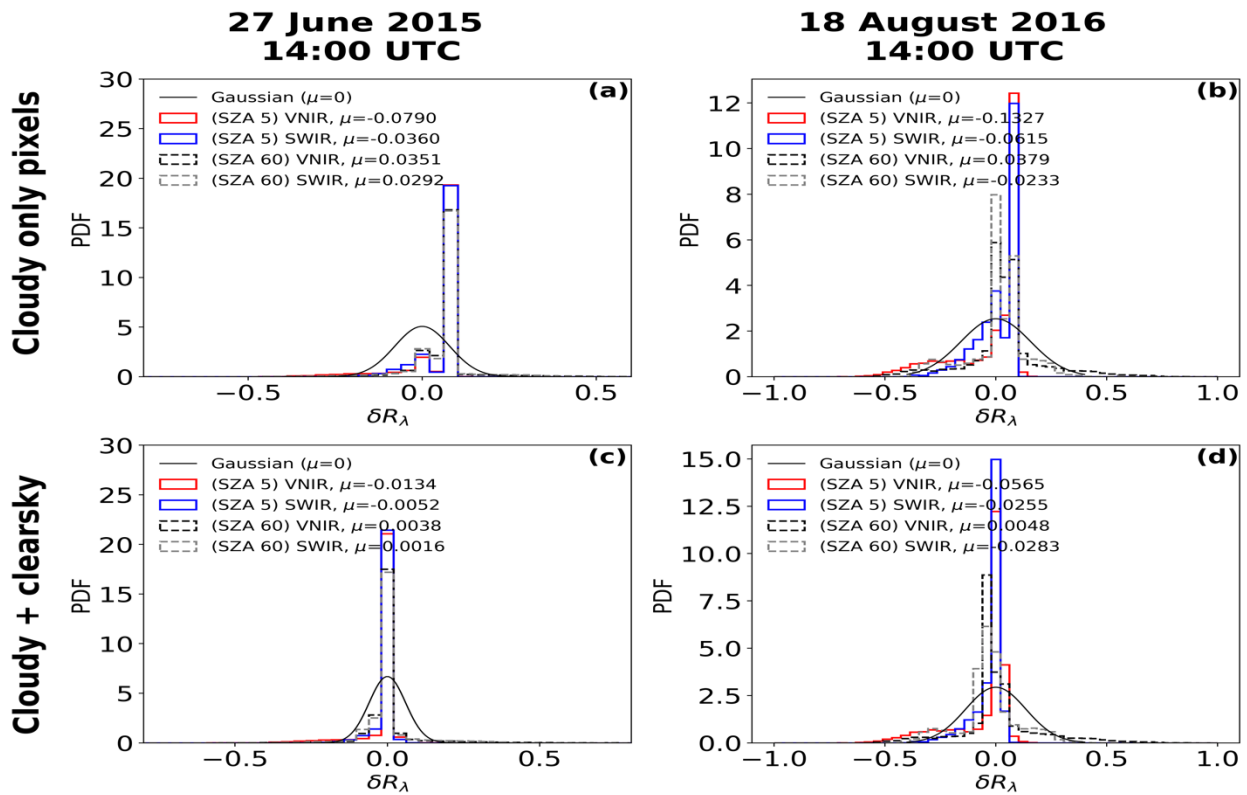
390   Fig. 5. PDF (Probability density function) of reflectance bias (δR) for cloudy only pixels for the 27 June case (a) and 18 August case
391   (b).   PDF of reflectance bias for cloudy and clear-sky pixels for the 27 June case (c) and 18 August case (d). μ is the domain mean
392   reflectance bias. A gaussian distribution (solid black curve) with standard deviation for the 0.66 μ m band at SZA 5 degrees and
393   centered around zero is shown in all panels.

394   Similar to the low sun case, the PDF of δR when both cloudy and clear-sky pixels for the high sun
395   case are considered (red and blue solid lines in **Fig. 5c, d**), shows a significant distribution of values close
396   to zero. Due to the leaking of photons from thick clouds to thin clouds and clear-sky regions surrounding
397   the clouds, there is an increase in the 3D reflectance of clear-sky regions. Additionally, when the sun is
398   high at SZA of $5°$, there are very minimal shadows cast on the clear-sky regions. These two highlighted
399   reasons result in a positive δR for the clear-sky only region. Thus, the negative value of δR for the cloudy

400   and clear-sky (same sign as the cloudy only) indicates that the domain scale reflectance bias is dominated
401   mainly by the cloudy only pixels and they play a significant role in the domain-scale statistics.

402

3.2. Investigating the 3D radiative effects on cloud retrievals

404   Focusing on SQ 2 in this section, we investigate how δR, as discussed in the previous section, affect
405   r_e and τ retrievals (i.e., Box A vs. Box D in the framework of **Fig. 1**). We utilize R_{1D} as inputs for the LUT
406   (explained in Sect. 2.3) to retrieve the 1D RT-based cloud droplet effective radius ($r_e^*(R_{1D})$) and cloud
407   optical thickness ($\tau^*(R_{1D})$). Additionally, we use R_{3D} as inputs for the LUT to retrieve the 3D RT-based
408   cloud droplet effective radius($r_e^*(R_{3D})$) and cloud optical thickness ($\tau^*(R_{3D})$).

409   Before discussing analysis of the 3D and 1D RT-based retrievals comparison, we first check the accuracy
410   of our retrievals by comparing the original LES cloud properties with our 1D RT-based retrievals (i.e.,
411   comparing retrievals from 1D radiance in Box C with cloud properties in Box A in **Fig. 1**). For this purpose,
412   the τ from the original LES (τ^{true}) is the vertical integration of the visible (0.66 μm) extinction coefficient
413   of each column from cloud base to cloud top. For the LES r_e, we follow Zhang et al. [2017] analytical
414   vertical weighting function (see their equation 4) to get the vertically weighted cloud droplet effective
415   radius (r_e^{VW}) where the $\mu_o = 0.5$, $\mu=1$ and the vertically weighting function parameter (b) associated with
416   the 2.13 μm band was set to 2 to allow for a deeper penetration depth and for better correlation between
417   the r_e^{VW}(2.13 μm) and bi-spectral retrievals.

418   **Fig. 6** shows the comparison between the r_e^{VW}(2.13 μm) and the $r_e^*(R_{1D})$ as well as τ^{true} with the
419   $\tau^*(R_{1D})$ for the two cloud fields at SZA=60$^°$ and VZA=0$^°$. For this comparison, the mean τ and r_e biases
420   are $\mu_{\tau\,bias} = \langle \tau^*(R_{1D}) - \tau^{true} \rangle$ and $\mu_{r_e\,bias} = \langle r_e^*(R_{1D}) - r_e^{VW}(2.13\,\mu m) \rangle$

421
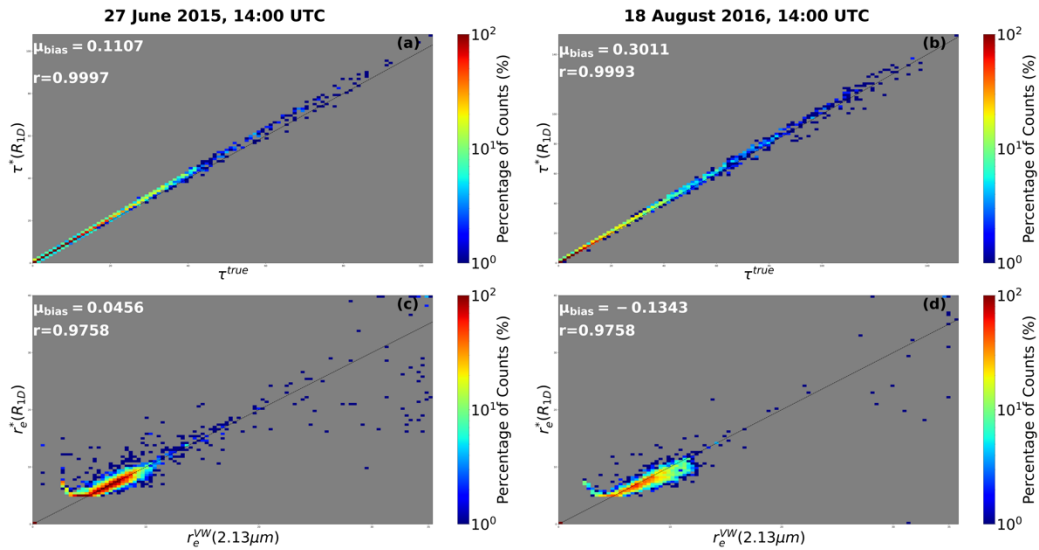
Fig. 6. Joint histogram of bi-spectral retrieved τ based on 1D RT simulated reflectance $\tau^*(R_{1D})$ vs Vertically integrated τ (τ^{true})
for the 27 June case (a) 18 August case (b). Joint histogram of bi-spectral retrieved r_e based on 1D RT simulated reflectance
($r_e^*(R_{1D})$) vs. vertically weighted effective radius (r_e^{VW}(2.13 μm)) in (c) and (d) $\mu_{bias} = \langle$retrieved cloud property $-$
reference cloud property$\rangle$.

For the two cloud fields considered in this study, the $\tau^*(R_{1D})$ is highly correlated with the τ^{true} as seen in the joint histogram plots (**Fig. 6a** and **b**) with a correlation coefficient (r) of 0.9997 for the 27 June case, and a r of 0.9993 for the 18 August case, although both have a slight positive mean bias ($\mu_{\tau\,bias} = 0.1107$ and 0.3011 for the 27 June and 18 August cases respectively). Also, the comparisons of the $r_e^*(R_{1D})$ with the $r_e^{VW}(2.13\,\mu m)$ in **Fig. 6c** and **d**, shows good correlation (r > 0.96) for both cloud cases, and slightly positive mean biases ($\mu_{r_e\,bias} = 0.0456$) for the 27 June case and a negative mean bias ($\mu_{r_e\,bias} = -0.1343$) for the 18 August case. Certain extreme outliers bias is observed in the r_e comparisons, these outliers are attributed to thin clouds and have been studied by Miller et al. [2018]. Several studies [e.g., Miller et al., 2016, 2018; Zhang et al., 2012] have investigated the accuracy of 1D bi-spectral retrievals compared to vertically weighted retrievals as well as the impact of cloud vertical profile on bi-spectral retrievals. Since we have good agreement between retrievals from the 1D RT-based reflectance and the original LES cloud field properties, this study will use the $r_e^*(R_{1D})$ and $\tau^*(R_{1D})$ as the reference cloud properties and directly compare them with the $r_e^*(R_{3D})$ and $\tau^*(R_{3D})$ to investigate the impacts of 3D radiative effects on the retrievals.

In the high sun case retrievals, $r_e^*(R_{3D})$ are overestimated and $\tau^*(R_{3D})$ are underestimated compared to their 1D counterpart. This is because photons leaking from optically thick regions to optically thin cloudy regions and out of cloud sides down to the surface where they are absorbed, results in a net photon loss which make the 3D radiance field appear darker than its 1D counterpart (explained in Sect. 3.1). Consequently, for retrievals, darkening shifts the reflectance observation on the LUT space leftwards and downwards to regions where the LUT r_e grid isolines represent larger droplet sizes and the LUT τ isolines represents thinner clouds. For the low sun case, $r_e^*(R_{3D})$ are underestimated and $\tau^*(R_{3D})$ overestimated in brightened optically thick cloudy pixels (facing the sun) and $r_e^*(R_{3D})$ are overestimated and $\tau^*(R_{3D})$ underestimated in darkened pixels on its opposite cloud side. Larger $r_e^*(R_{3D})$ and smaller $\tau^*(R_{3D})$ compared to $\tau^*(R_{1D})$ and $\tau^*(R_{1D})$ in brightened pixels occurs since brightening phenomena in the LUT space shifts the observed reflectance upwards and rightwards where the LUT r_e grid isolines represents smaller droplets sizes and the LUT τ isolines represents thicker clouds. τ and r_e retrieval biases in satellite observations have been well documented in numerous studies [e.g., Várnai and Marshak, 2002; Zhang and Platnick, 2011; Zhang et al., 2012], and in common occurrence, overestimation of $\tau^*(R_{3D})$ is coupled with the underestimation of $r_e^*(R_{3D})$ and vice versa.

Table 2 shows the frequency of failed and successful retrievals from R_{3D} for the two cloud fields considered in this study. It is observed that the number of failed retrievals is small for the SZA 5° case (< 13%), while the retrieval failures are larger for the SZA 60° case (> 40%) for both cloud fields under consideration. The larger retrieval failures for the low sun case is mostly attributed to multiple scattering in the 3D RT due to increased path length (since original direction of travel of the photons from the sun is oblique), which increases radiation-cloud interaction and reflectance. Although, this leads mostly to τ failures, the other r_e type failures can arise from very darkened pixels (from photon leaking or cloud shadow) which shifts observation outside the LUT lower range (for r_e too large) or brightened pixels from less absorbing clouds which shifts the observations beyond the upper range of the LUT (for r_e too small) depending on the scenario.

Table 2. Statistics of successful and failed retrievals from the 3D RT-based radiance for the 27 June and 18 August cloud fields at Solar zenith angle (SZA) 5 and 60 degrees. The columns from left to right are Case name (Identified by date and time), solar zenith

Case name	SZA	No of pixels with successful retrievals only	Pixels with failed retrievals			Total number of successful and failed pixels
			Category of failed retrievals	No of pixels	Total	
27 June 2015, 14:00 UTC	5°	3670 (87.82%)	r_e too large	85 (2.03%)	509 (12.17%)	4179 (100%)
			r_e too small	365 (8.73%)		
			τ failures	63 (1.41%)		
	60°	2100 (50.16%)	r_e too large	97 (2.32%)	2079 (49.74%)	4179 (100%)
			r_e too small	1035 (24.77%)		
			τ failures	947 (22.66%)		
18 August 2016, 14:00 UTC	5°	2344 (96.02%)	r_e too large	46 (1.88%)	97 (3.97%)	2441 (100%)
			r_e too small	29 (1.188%)		
			τ failures	22 (0.90%)		
	60°	1368 (56.04%)	r_e too large	339 (13.88%)	1073 (43.96%)	2441 (100%)
			r_e too small	178 (7.29%)		
			τ failures	556 (22.77%)		

Values in parentheses are percentage of counts. (Percentage of counts = Number of affected pixels/ Total number of pixels)

470

3.3. Investigating the 3D radiative effects on the Broadband radiative flux

472

3.3.1. Investigating the 3D radiative effects on the broadband radiative flux: Using a combination of the successful and failed retrievals as the input cloud property

475 Focusing on SQ 3 in this section, we will compare F_{3D} and F_{1D}^* to investigate the impact of cloud
476 retrieval biases due to the 3D radiative effects on the broadband SW radiative flux. We will also compare
477 F_{3D} and F_{1D}^* to study the impact of neglecting horizontal photons transport on the broadband SW flux
478 results. Additionally, we compare δF_1 (i.e., $F_{3D} - F_{1D}^*$) with δF_2 (i.e., $F_{3D} - F_{1D}$) to determine errors in
479 radiative flux estimates and evaluate the CRE.

480 It is important to note here that both the successful and the failed retrievals as described in Sect.
481 2.4 are included in the RT simulations in the control simulations presented in this section. The motivation
482 for including the failed retrievals is to preserve the impacts of this significant fraction of pixels on the
483 domain averaged fluxes and CRE simulations, even though the retrieval of τ and r_e based on the bi-
484 spectral method fails for them. In addition to the controlled simulations, we have also conducted
485 sensitivity studies, where we exclude the failed retrievals in the analysis. The results are shown and
486 discussed in the Appendix.

487 Maps of the simulated SW broadband radiative quantities (reflected flux at the TOD ($F^\uparrow$),
488 transmitted flux at the surface ($F^\downarrow$), and column absorbed flux (F^{abs})) for the 27 June case at the high and
489 low sun angles are presented in **Fig. 7** and **Fig. 8**, respectively. These figures reveal several interesting and
490 important points. First, it is interesting to note that the reflected flux in **Fig. 7d** seems blurry in comparison
491 with 1D results in **Fig. 7a** and **Fig. 7g**. The same is also seen comparing **Fig. 8d** with **Fig. 8a** and **Fig. 8g**. This
492 is because in 1D RT, simulation of the upwelling hemispheric flux at a given point at the TOD is determined
493 *only* by the cloud and surface properties in the column beneath such point. In contrast, in 3D RT

494   simulation, it depends on the cloud and surface properties of both the corresponding column and a large
495   extent of the surrounding columns, as a result of simple parallax effect. Therefore, the contrast between
496   two adjacent columns in the 1D simulation, for example, a cloudy column and an adjacent clear-sky
497   column next to it, is quite large, whereas the contrast for the same two columns in 3D simulation is much
498   smaller because the two have a significant overlap in terms of the areas that have influences on their flux.
499   Because of this fundamental difference between 1D and 3D simulations, a pixel-to-pixel comparison of
500   the upwelling flux is not appropriate. Instead, we compare the domain-averaged statistics.
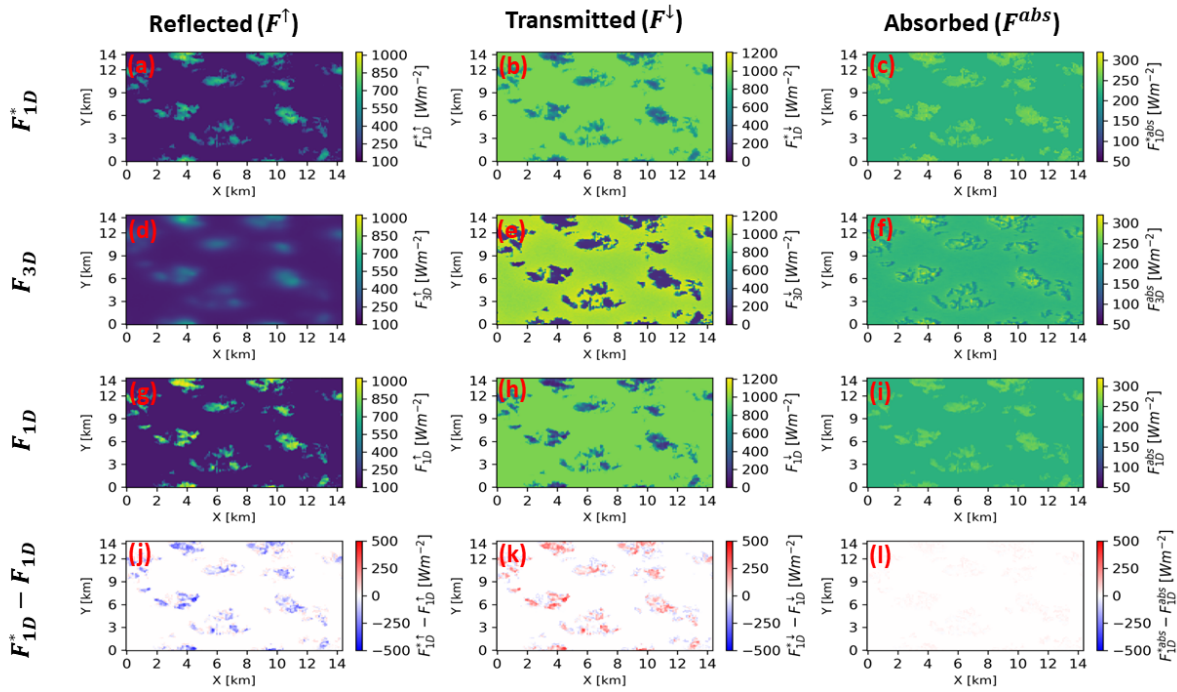
501

502   **Fig. 7.** Simulated shortwave broadband Reflected flux at top of the domain ($F^{\uparrow}$), Transmitted flux at the surface ($F^{\downarrow}$) and Column
503   absorbed flux (F^{abs}) derived from the retrieved clouds properties using 1D RT, F^{*}_{1D} (a)-(c), derived from the true clouds properties
504   using 3D RT, F_{3D} (d)-(f), derived from the true clouds properties using 1D RT, F_{1D} (g)-(i) and difference between F^{*}_{1D} and F_{1D} (j)-
505   (l) for Solar zenith angle=5° and View zenith angle=0°. Sun is high and slightly on the Left-hand side of the domain. The solar
506   irradiance at the top of the domain scales with the cosine of the solar zenith angle.

507   Before we delve into that, we first aim to unravel how cloud property retrieval errors affect 1D RT flux
508   solutions. For this purpose, we compare the $F^{\uparrow}$ component of F^{*}_{1D} (denoted by $F^{*\uparrow}_{1D}$) with the $F^{\uparrow}$
509   component of F_{1D} (denoted by $F^{\uparrow}_{1D}$). The same comparison is done between the $F^{\downarrow}$ component of F^{*}_{1D}
510   (denoted by $F^{*\downarrow}_{1D}$) and its counterpart from the F_{1D} (denoted by $F^{\downarrow}_{1D}$). The $F^{*\uparrow}_{1D}$ have visible signatures of
511   the input cloud property retrievals. For instance, in the high sun case, smaller reflected flux values (recall,
512   underestimated τ dominates retrievals from high sun radiance) dominate $F^{*\uparrow}_{1D}$ (**Fig. 7a**) as compared to
513     $F^{\uparrow}_{1D}$ (**Fig. 7g**) . The underestimation of $F^{*\uparrow}_{1D}$ compared to $F^{\uparrow}_{1D}$ is evident in **Fig. 7j**. This difference is also well
514   captured in the domain-averaged values which will be discussed later in this section. In the low sun case,
515   comparison between $F^{*\uparrow}_{1D}$ and corresponding $F^{\uparrow}_{1D}$ reveals that in $F^{*\uparrow}_{1D}$, the overestimated retrieved τ areas
516   characterized by thicker clouds (i.e., retrieved from brightened pixels) provides larger reflected flux values
517   and the underestimated retrieved τ areas characterized by thinner clouds (i.e., retrieved from darkened
518   pixels) have smaller reflected flux values than their $F^{\uparrow}_{1D}$ counterpart (**Fig. 8j**). Their overall effect on the

519 domain reflected flux values depends on how the opposite 3D radiative effects (cloud side brightening
520 and darkening) mitigate each other.

521
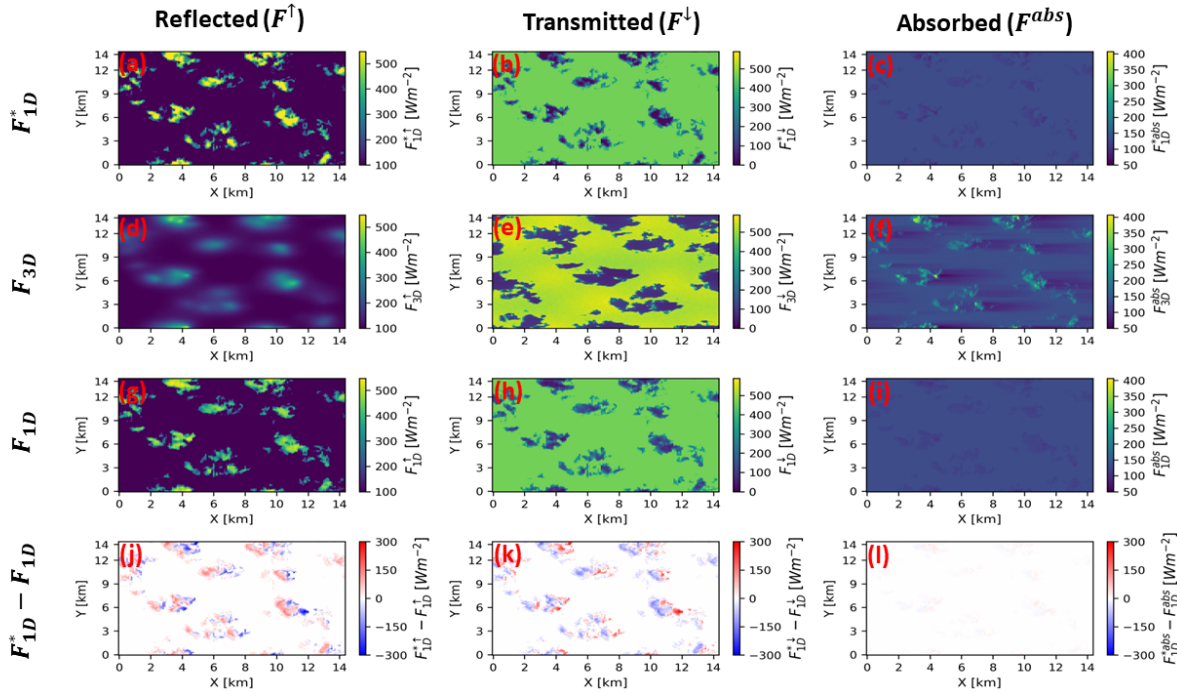
523 **Fig. 8.** Simulated shortwave broadband Reflected flux at top of the domain ($F^\uparrow$), Transmitted flux at the surface ($F^\downarrow$) and
524 Column absorbed flux (F^{abs}) derived from the retrieved clouds properties using 1D RT, F^*_{1D} (a)-(c), derived from the true clouds
525 properties using 3D RT, F_{3D} (d)-(f), derived from the true clouds properties using 1D RT, F_{1D} (g)-(i) and difference between F^*_{1D}
526 and F_{1D} (j)-(l) for Solar zenith angle=60° and View zenith angle=0°. Sun is on the Left-hand side of the domain. The solar
527 irradiance at the top of the domain scales with the cosine of the solar zenith angle.

528 An examination of $F^\downarrow_{1D}$ and $F^{*\downarrow}_{1D}$ for the high sun case reveals that $F^{*\downarrow}_{1D}$ beneath clouds is larger compared
529 to $F^\downarrow_{1D}$, while they have same values in clear-sky regions (**Fig. 7k**) This is expected since $F^{*\uparrow}_{1D}$ is lesser than
530 $F^\uparrow_{1D}$. Thus, the amount of $F^{*\downarrow}_{1D}$ at the surface beneath the cloud increases. For the low sun case, $F^\downarrow_{1D}$ and
531 $F^{*\downarrow}_{1D}$ beneath the clouds have higher values where the TOD reflected flux is low and lower values where
532 the TOD reflected flux is high (**Fig. 8k**).

533 The radiative quantities across the LES domain have different characteristics in F_{3D} stemming from the
534 horizontal transport of photons across pixels. For the high sun case, aside the blurriness of the $F^\uparrow$
535 component of F_{3D} (denoted by $F^\uparrow_{3D}$) which was previously explained, an examination of the $F^\downarrow$
536 component of F_{3D} (denoted by $F^\downarrow_{3D}$) map in **Fig. 7e** shows a slight tilt of the cloud shadows according to
537 the angle of projection of the sun (located at SZA 5° to the left). It also reveals enhanced $F^\downarrow_{3D}$ values
538 around cloud edges. Such is not the case in $F^\downarrow_{1D}$ (**Fig. 7h**) due to 1D RT setup where each cloudy column is
539 considered independent. These observations are consistent with findings made by Gristey et al. [2020] for
540 similar shallow cumulus cloud fields. Gristey et al. [2020], showed that these enhanced $F^\downarrow_{3D}$ around cloud
541 edges is primarily caused by the diffused component of the transmitted flux which are scattered by clouds
542 towards clear sky regions beyond cloud shadows. In $F^\downarrow_{3D}$ for the low sun (**Fig. 8e**), due to 3D RT and the
543 more oblique solar angle (SZA 60°), there is an increase in the total effective cloud cover [Di Giuseppe and

544 Tompkins, 2003; Tompkins and Di Giuseppe, 2007], as well as an increase in the size of the cloud shadow,
545 which reduces the transmitted flux at the surface (e.g., around [X=7,Y=6 km] in **Fig. 8e**. Just as in the case
546 of the high sun, these features are absent in the low sun 1D RT runs ($F_{1D}^{*\downarrow}$ and $F_{1D}^{\downarrow}$). An analysis of the
547 domain-averaged statistics will help shed more light on the differences between the 3D RT and 1D RT
548 radiative flux results on the domain scale.

549 **Table 3**. Statistics of successful and failed retrievals from the 3D RT¬ based radiance for the 27 June and 18 August cloud fields
550 at Solar zenith angle (SZA) 5 and 60 degrees. The columns from left to right are Case name (Identified by date and time), solar
551 zenith angle (SZA), Number of pixels with successful retrievals only, Pixels with failed retrievals, Total number of successful and
552 failed retrievals.

Case Name		SZA 5 degrees			SZA 60 degrees		
		F_{1D}^{*} (Wm^{-2})	F_{3D} (Wm^{-2})	F_{1D} (Wm^{-2})	F_{1D}^{*} (Wm^{-2})	F_{3D} (Wm^{-2})	F_{1D} (Wm^{-2})
27 June 2015 **(14:00 UTC)**	$F^{\uparrow}$	215.44 (213.94)	215.93	225.37 (223.52)	134.22 (111.21)	137.87	133.04 (112.01)
	$F^{\downarrow}$	918.97 (920.68)	918.79	910.76 (912.88)	419.60 (441.77)	414.36	420.97 (441.34)
	F^{abs}	228.56 (228.37)	228.23	226.82 (226.60)	130.25 (131.13)	131.82	130.11 (130.79)
18 Aug. 2016 **(14:00 UTC)**	$F^{\uparrow}$	315.16 (316.82)	308.68	355.26 (357.12)	209.74 (174.40)	218.62	211.54 (171.59)
	$F^{\downarrow}$	805.34 (803.59)	812.25	770.21 (768.26)	342.50 (378.46)	326.53	341.92 (382.68)
	F^{abs}	242.36 (242.48)	241.95	237.36 (237.46)	131.74 (131.20)	138.86	130.55 (129.76)

Note: Values before the parentheses are calculated from the combination of failed and successful retrievals representing the total
cloudy population, while values in parentheses are calculated from successful retrievals only representing the total cloudy population.
clear-sky pixels values have been included in all calculations.

553

554   The domain-averaged broadband $F^{\uparrow}$, $F^{\downarrow}$ and F^{abs} components of F_{1D}^{*}, F_{1D} and F_{3D} for the 27
555 June and 18 August cases at SZA 5° and SZA 60° are reported in **Table 3**. As previously explained, the
556 predominant photon leaking associated with high sun 3D RT and the ensuing underestimation of the
557 retrieved τ which dominate the cloud property retrievals from high sun 3D simulated reflectance,
558 increases the number of retrieved optically thinner clouds (relative to the original LES τ used in F_{1D}
559 calculations) utilized as inputs for the F_{1D}^{*} calculations. This leads to the underestimation of the
560 domain-averaged $F_{1D}^{*\uparrow}$ compared to $F_{1D}^{\uparrow}$; In the 27 June case, the domain-averaged $F_{1D}^{*\uparrow}$ (215.44 Wm^{-2})
561 is underestimated compared to the corresponding $F_{1D}^{\uparrow}$ value (225.37 Wm^{-2}) by about 9.93 Wm^{-2}. While
562 in the 18 August case, the domain-averaged $F_{1D}^{*\uparrow}$ (315.16 Wm^{-2}) is underestimated compared to the
563 corresponding $F_{1D}^{\uparrow}$ value (355.26 Wm^{-2}) by 40.1 Wm^{-2}. The larger value of the underestimated
564 domain-averaged $F_{1D}^{*\uparrow}$ in the 18 August case stems from its larger cloud fraction and τ bias. The
565 transmitted flux at the surface below clouds is dependent on the amount of flux reflected towards the
566 TOD; lower reflected flux values indicate that less radiation is reflected from the clouds, which allows for
567 a greater amount of radiative flux to be transmitted to the surface beneath the clouds. This reason,
568 coupled with the overestimation of the transmitted flux at the surface due to missed thin clouds in our
569 bi-spectral retrievals (red regions in **Fig. 3**, retrieved $\tau = 0$ for VNIR reflectance less than the smallest LUT
570 τ value), explains why for the high sun case, the domain-averaged $F_{1D}^{*\downarrow}$ values are higher compared to $F_{1D}^{\downarrow}$
571 values, resulting in differences of 8.21 Wm^{-2} and 35.13 Wm^{-2} for the 27 June and 18 August cases
572 respectively. Although, for the high sun angle, the contribution of the missed thin clouds to the
573 overestimation of $F_{1D}^{*\downarrow}$ beneath clouds in our case study is small (Constituting about 0.23% and 0.34% of
574 the domain-averaged surface transmitted flux for the 27 June and 18 August high cases respectively).

575   Comparing results from the three sets of experiments in **Table 3** reveals that for the high sun case,
576 the F_{1D}^{*} results clearly agree better with the benchmark F_{3D}, than the F_{1D} results. In the 27 June case, δF_{1}

577 for the domain-averaged $F^\uparrow$, $F^\downarrow$ and F^{abs} are 0.49, −0.18 and −0.33 Wm^{-2} respectively, which are
578 significantly smaller in magnitude than those for δF_2 (−9.44, 8.03, and 1.41 Wm^{-2} respectively). Similarly,
579 for the 18 August case, δF_1 for the domain-averaged $F^\uparrow$, $F^\downarrow$ and F^{abs} are −6.48, 6.81 and −0.41 Wm^{-2}
580 respectively compared to corresponding biases of −46.58, 42.04, and 4.59 Wm^{-2} for δF_2. These results
581 suggests that F_{1D}^* gives an overall better radiative energy estimate than F_{1D} for the high SZA case. In the
582 low sun case, the F_{1D}^* and F_{1D} are very close to each other and there is no clear winner when compared
583 to the benchmark 3D RT results. In the 27 June case, the F_{1D}^* agrees slightly better with 3D results than
584 the F_{1D}, but the opposite is true in the 18 August case. This result seems to suggest that although in the
585 low sun case the brightening and darkening effects can lead to large retrieval biases, they tend to cancel
586 out each other in the flux computations. Interestingly, both 1D results tend to underestimate $F^\uparrow$ and
587 overestimate $F^\downarrow$. This is probably because the brightening effect is dominant in the 3D RT leading to some
588 extremely bright pixels. But they are not captured in the 1D RT computations, even in the F_{1D}^* using the
589 upper limit of τ=158.48 in the flux computation. Thus, the reflected flux quickly reaches the asymptotic
590 value when τ is large and therefore simply using larger τ value in 1D RT cannot simulate the extreme
591 brightness of clouds due the brightening effect in 3D RT. Results for δF_2 computed from the transmitted
592 flux at the surface for both cloud cases (27 June and 18 August) are positive when the sun is high (8.03
593 and 42.04 Wm^{-2}) and negative for the low sun angle (−6.61 and −15.39 Wm^{-2}) consistent with Gristey
594 el al. [2020] study for surface irradiance showing positive domain mean δF_2 in the afternoon (high sun)
595 and negative domain mean δF_2 towards the end of the day (low sun).
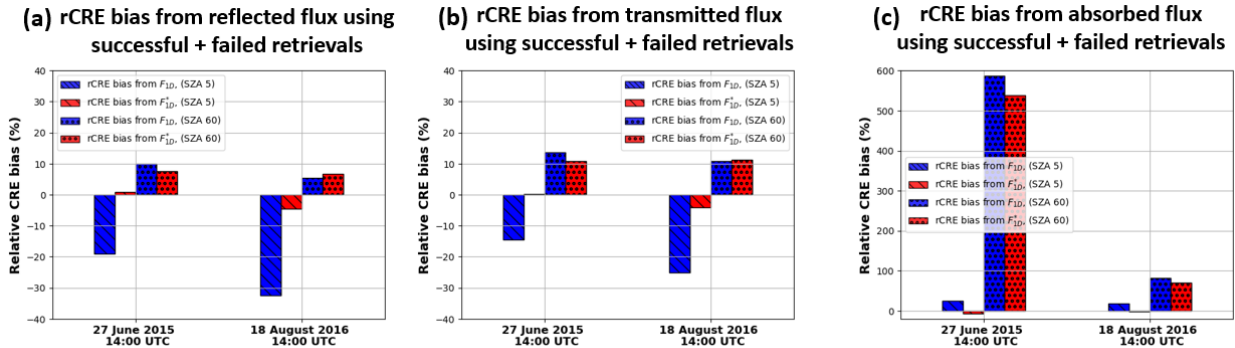
596

597 **Fig. 9.** Relative cloud radiative effect (rCRE) bias computed from the successful + failed retrievals (a) top of the domain
598 reflected, (b) surface transmitted and (c) absorbed flux for the two cloud fields.

599 Because both cloud cases have a cloud fraction lower than 50%, the domain-averaged statistics
600 include a large fraction of clear-sky pixels. Now we focus our scope on cloudy pixels and investigate the
601 differences in CRE. The rCRE bias provides a quantitative estimate of how these biases affect the CRE. For
602 the two cloud cases considered in this study, plots of rCRE bias computed from the $F^\uparrow$, $F^\downarrow$ and F^{abs} at SZA
603 5° and 60° for F_{1D}^* and F_{1D} relative to F_{3D} are presented in **Fig. 9**. In the 27 June case, the rCRE bias of
604 0.97% computed from the high sun $F_{1D}^{*\uparrow}$ result indicate a negligible deviation (less than 1%) from the
605 benchmark CRE while the rCRE bias of −19% computed from the high sun $F_{1D}^\uparrow$ result show that the bias
606 is quite substantial. Similarly, for the 18 August case, the rCRE bias computed from the high sun $F_{1D}^{*\uparrow}$ result
607 is less than 5%. On the other hand, the rCRE bias of −32.48% computed from the high sun $F_{1D}^\uparrow$ result
608 show that the bias is quite large. Similar results are obtained for rCRE bias computed from $F^\downarrow$. In the 27
609 June case, the rCRE bias computed from the $F_{1D}^{*\downarrow}$ is 0.33% (**Fig. 9b**, second bar on the left) which shows

610 minimal bias less than 1%, while the rCRE computed from the $F_{1D}^{\downarrow}$ is -14.5% (**Fig. 9b**, first bar on the left).
611 Similarly, for the 18 August case, the rCRE bias computed from the $F_{1D}^{*\downarrow}$ is -4.12% (**Fig. 9b**, second bar on
612 the right), while the rCRE bias computed from the $F_{1D}^{\downarrow}$ is -25.10% (**Fig. 9b**, first bar on the right).

613 When the absorbed flux is taken into consideration, for the 27 June high sun case, the rCRE bias computed
614 from the absorbed component of F_{1D}^{*} (F_{1D}^{*abs}) is -6.05% (**Fig. 9c**, second bar on the left) which is less bias
615 compared to the 25.64% rCRE bias computed from the absorbed component of F_{1D} (F_{1D}^{abs}) (**Fig. 9 c**, first
616 bar on the left). Similarly, for the 18 August case, the rCRE bias computed from F_{1D}^{*abs} is -1.73% (**Fig. 9c**,
617 second bar on the right), while the rCRE bias computed from F_{1D}^{abs} is 19.09% (**Fig. 9c**, first bar on the right).
618 For the low sun case, the rCRE biases computed from F_{1D}^{*} and F_{1D} are comparable, which is consistent
619 with the domain-averaged statistics in **Table 3**. Evidently, both F_{1D}^{*} and F_{1D} overestimate the CRE at TOD
620 and surface, which means an underestimation of cloud reflection and overestimation of transmission. This
621 is consistent with the results in **Table 3**.

622 Overall, the above analysis indicates that the F_{1D}^{*} provides a better (in the high sun case) or at least
623 comparable (in the low sun case) results than F_{1D} for both domain-averaged flux statistics and CRE when
624 compared to the benchmark F_{3D} results. With these results we can conclude that the CRE calculated with
625 1D RT using retrieved cloud properties which are biased due to the 3D effects is found to be comparable
626 or better than the CRE calculated with 1D RT using the true cloud properties.

627 **4. Summary and Conclusion**

628   It is well known that the bi-spectral cloud property retrievals based on the 1D RT have significant
629 errors due to the 3D radiative effects. In this study, we investigate whether the biased retrievals can still
630 be used to estimate the broadband flux and CRE. To address this question, we selected two cloud fields
631 from the LASSO activity: one on 27 June 2015 and another on 18 August 2016 to serve as case studies for
632 our research. The LES cloud fields have different microphysics with different CBH, CTH and the value of
633 the cloud fraction for the 18 August 2016 cloud field (47.08%) is more than twice that of the 27 June 2015
634 (20.15%) cloud field. Radiance simulations, bi-spectral retrievals, and broadband SW flux radiative transfer
635 simulations were performed using these cloud fields at two SZAs, a high sun case (SZA=5°) and a low sun
636 case (SZA=60°) and the results were analyzed. The flux computations were carried out in three sets, the
637 reference broadband SW flux calculations were performed using the cloud properties from the original
638 LES cloud field under 3D RT (F_{3D}), we also computed similar RT broadband SW flux calculations with the
639 same cloud properties from the original LES cloud field except that the RT calculations were computed
640 using 1D RT (F_{1D}). Additionally, we computed the last set of broadband SW flux calculations using 1D RT
641 and bi-spectrally retrieved cloud properties as inputs (F_{1D}^{*}).

642   The high sun radiance results, for the two cloud fields show that in 3D RT high sun case, the photons
643 leaking from optically thick cloudy regions to optically thin cloudy regions and surface dominate the LES
644 reflectance field. These results in overestimated r_e and underestimated τ dominating the cloud property
645 retrievals. While results from the low sun case, for the two cloud fields considered show that in
646 comparison to the 1D RT radiance fields, brightening and darkening effects both occur in the 3D RT
647 simulated radiance observation. Therefore, retrievals from the low sun 3D radiance observations are
648 characterized mainly by both overestimation of τ and underestimation of r_e in brightened pixels and
649 underestimation of τ and overestimation of r_e in darkened pixels. The cumulative effects of these

650 brightening and darkening/Photon leaking effects and its impacts on the retrieved cloud properties
651 dictates their impact on the broadband radiative flux.

652   The results from the broadband SW radiative fluxes computation showed that, although the
653 bi-spectrally retrieved cloud properties are often biased due to the 3D radiative transfer effects, for high
654 sun cases, calculations of the CRE from these F_{1D}^* values agree well with the benchmark values (which is
655 the F_{3D} in our case) with agreement within 7% for rCRE bias calculations from the reflected, transmitted
656 and absorbed fluxes in the high sun cases. Conversely, the rCRE bias computed from the F_{1D} quantities
657 could reach about 33%. Thus, for high sun situations, the F_{1D}^* provides consistently better estimates of
658 the CRE than the F_{1D}. For the low sun case, the two 1D RT experiments provide comparable results, both
659 underestimating cloud reflection and overestimating transmission, and there is not a clear winner when
660 compared to the 3D RT benchmark.

661   The influence of the failed retrievals on the CRE was also investigated (see details in Appendix),
662 with results indicating that for the high sun case, the impact of the failed retrievals on the radiative flux
663 quantities is negligible, with less than 6% changes observed in the rCRE bias computed from the
664 domain-averaged TOD reflected, surface transmitted and absorbed F_{1D}^* and F_{1D} results. Such is not the
665 case for the low sun case where the failed retrievals have a very huge impact on the radiative flux
666 quantities. Excluding the failed retrievals from the domain-averaged reflected, transmitted, and absorbed
667 F_{1D}^* and F_{1D} low sun case analysis could increase the rCRE bias by a as much as factor of 6 compared to
668 values which included the failed retrievals in the analysis. Whether or not to always use the failed
669 retrievals in the radiative flux and CRE estimation is still an important question, especially how best to
670 filter out the failed retrievals from cloud properties retrieved from instruments that rely on bi-spectral
671 method (e.g., in MODIS cloud products) for use in radiative flux estimation? We observed here that,
672 filtering out all failed retrievals, especially from the low sun angle can greatly impact the radiative flux
673 estimates. Thus, efforts should be conducted to study which category of failed retrievals is most relevant
674 for use in CRE estimation.

675   In conclusion, despite the potential biases due to the 3D radiative effects, the retrieved cloud
676 properties based on 1D RT from the bi-spectral method still provide CRE estimates that are comparable
677 to or better than CRE calculated from the true cloud properties using 1D RT. Some future questions that
678 warrant answers involves how the 3D radiative effects affect the broadband fluxes for different cloud
679 arrangements and other types of clouds, such as deep convective clouds. Also, while we have considered
680 only nadir view angle in this work, previous studies [e.g., Várnai and Marshak, 2007] have shown that the
681 biases of 1D cloud retrievals vary systematically with view direction, therefore, the impacts of off-nadir
682 view directions on the broadband flux need to be investigated. Another important study will be to
683 determine how changes in surface albedo and type affect our results. Additionally, while our case study
684 mainly focused on the impact of the 3D radiative effects on SW fluxes, the impact of the 3D radiative
685 effects on LW radiation is important and needs to be investigated.

686 **Appendix A: Impacts of failed retrievals on the radiative flux**

687   The calculations of F_{1D}^* and domain radiative flux analysis in Sect. 3.3 utilized both the successful
688 and failed retrievals (categorized in Sect. 2.4) to represent the total population of cloudy pixels.
689 Henceforth, both successful and failed retrievals as a representative of the total population of cloudy
690 pixels will be referred to as "all retrieved cloud pixels". In this appendix, our focus is to examine and

691 compare the TOD reflected, surface transmitted and column absorbed radiative fluxes, when the failed
692 retrievals are excluded from the radiative flux analysis. This will help to diagnose if using solely successful
693 retrievals as a representative of the total population of cloudy pixels in the LES domain will produce the
694 correct radiative energy estimates and thus provide information on the radiative properties of the
695 excluded failed retrievals.

696 An examination of the high sun domain-averaged $F^\uparrow$, $F^\downarrow$ and F^{abs} for both LES cloud cases, when
697 only successful retrievals represent the total population of cloudy pixels in the F^*_{1D} calculations, show
698 minimal changes (within the range $\pm 1.9\,\mathrm{Wm}^{-2}$) from previous values which utilized all retrieved cloud
699 pixels in the radiative flux analysis (**Table 3**). This is due to the small number of failed retrievals in the high
700 sun scenario (< 14% for both cloud cases; **Table 2**). But this is not the case for the low sun case, where
701 changes between the two aforementioned calculations are large, reaching up to $\pm 35.96\,\mathrm{Wm}^{-2}$ (**Table 3**).
702 These large changes are because of the large number of failed retrievals from strong 3D radiative effects
703 (> 43% for both cloud cases; **Table 2**) as well as different radiative behavior of the failed retrievals
704 categories observed in the low sun scenario. **Fig. A1** shows plots of successful and failed retrievals
705 categories (classified as described in Sect. 2.4) from the high and low sun radiance for the 27 June and 18
706 August cases. From these plots, it is observed that when the SZA is $60°$, the r_e too small failures are
707 predominant around cloud edges in the sunlit areas. The τ failures are observed mostly in the illuminated
708 sunlit cloudy regions and the r_e too large failures occur mostly on the opposite sides where the shadowing
709 effect is dominant (**Fig. A1b** and **d**). For the high sun at SZA $5°$, τ failures are almost negligible because the
710 VNIR reflectance observations does not exceed the LUT τ upper limit of 158.48, while there is a small
711 number of occurrences of the r_e too large and r_e too small failures (**Fig. A1a** and **c**).

712 It should be noted that when we exclude the failed retrievals from the broadband flux analysis,
713 we keep the total cloud fraction constant. In other words, we scale the broadband flux based on the
714 successful pixels by the ratio of total cloudy to successful pixels such that the effect of cloud fraction
715 reduction is removed from the analysis. The impacts of excluding failed retrievals on the domain-averaged
716 broadband flux can be assessed by comparing the values outside the parentheses with those inside in
717 **Table 3**, and better understood in the light of failed retrieval statistics given in **Table 2**.

718 Results of F^*_{1D} for the 27 June case at SZA $5°$, show that the domain‑averaged $F^{*\uparrow}_{1D}$ is
719 underestimated by $1.50\,\mathrm{Wm}^{-2}$ ($213.94\,\mathrm{Wm}^{-2}$ in comparison to $215.44\,\mathrm{Wm}^{-2}$) when only successful
720 pixels are used to represent the total population of cloudy pixels compared to results which utilize all
721 retrieved cloud pixels in the radiative flux analysis. This is mainly because the dominant type of retrieval
722 failure in this case is the r_e too small failure, accounting for about 71% of the failed pixel retrieval statistics
723 (see **Table 2**). Recall that r_e too small failure is mainly a result of brightening effect and therefore
724 associated pixels appear brighter in 3D RT than 1D RT. As a result, excluding these pixels leads to an
725 underestimate of domain-averaged broadband reflected flux. For the same reason, excluding these pixels
726 leads to an overestimation of transmitted flux at the domain bottom.

727 In contrast to the 27 June case, excluding the failed retrievals in the F^*_{1D} for the 18 August case
728 leads to an overestimation of domain-averaged $F^{*\uparrow}_{1D}$ and underestimation of the $F^{*\downarrow}_{1D}$. This is probably
729 because the dominant failed retrieval type is the r_e too large which is because of the darkening effect.
730 These pixels appear darker from the perspective of TOD and more transmissive from the perspective of
731 bottom in 3D RT than 1D RT. For comparison purpose, we have also excluded the failed pixels from the
732 F_{1D} calculations. Overall, the results are very similar and consistent with those based on F^*_{1D}.
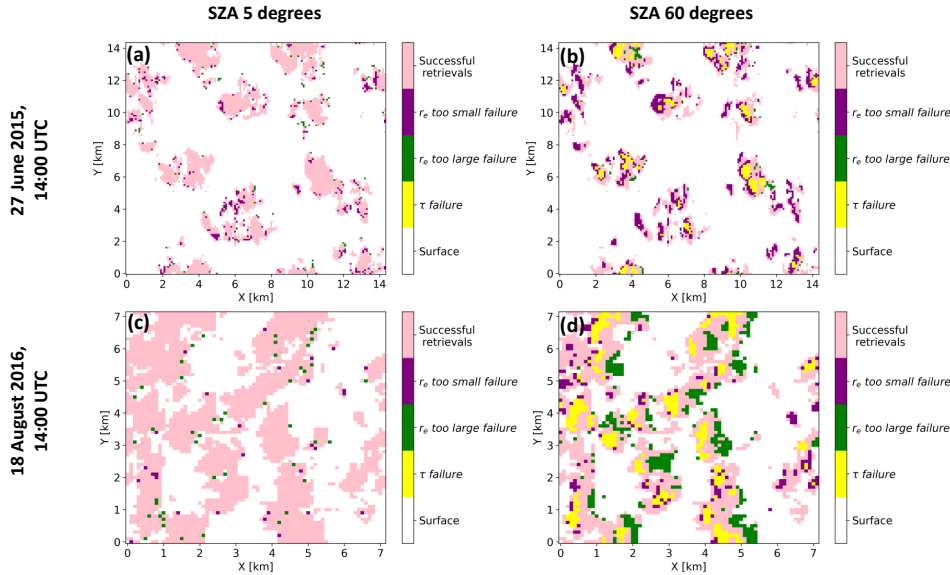
Fig A1. Plots of successful and failed retrievals categories for the 27 June 2015 and 18 August 2016 cases at Solar zenith angle 5 degrees (a and c) and Solar zenith angle 60 degrees (b and d).

In comparison with the high sun case, the impacts of failed retrievals on the broadband flux statistics are much larger in the low sun SZA 60° case. In both LES cases, the exclusion of failed retrievals leads to a significant decrease of domain-averaged $F_{1D}^{*\uparrow}$ and increase of the $F_{1D}^{*\downarrow}$. For example, in the 27 June case, the $F_{1D}^{*\uparrow}$ decreased from 134.22 Wm^{-2} when failed pixels are included to 111.21 Wm^{-2} when they are excluded, which is accompanied by an increase of the $F_{1D}^{*\downarrow}$ from 419.60 Wm^{-2} to 441.77 Wm^{-2}. A close look at **Table 2** reveals that in both LES cases, the combination of r_e too small and τ failures accounts for the majority of failed retrievals, 95% in the case of 27 June and 68% in the 18 August case. As mentioned above, both types of failures are because of the brightening effect. Excluding them is expected to cause underestimation of domain-averaged reflected flux and overestimation of the transmitted flux.
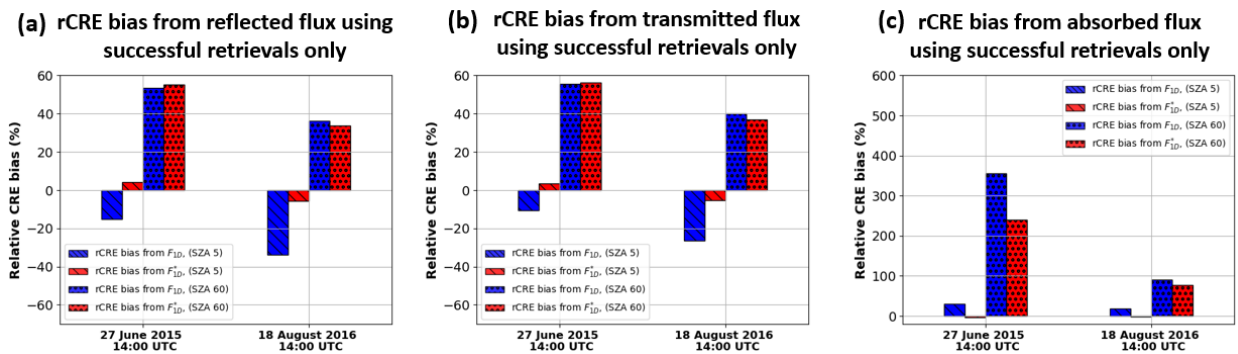
Fig.A2. Relative cloud radiative effect bias computed from the successful only retrievals, top of the domain reflected in (a), surface transmitted in (b) and column absorbed flux in (c) for the two cloud fields.

The impacts of excluding failed retrievals on the rCRE bias are shown in **Fig. A2**. A comparison to the results in **Fig. 9** reveals two points. First, the biases in the low sun cases become much larger which is expected because there are much more failed retrievals in these cases. Second, it is evident that the flux

752 estimates derived from the retrieved clouds using 1D RT still provide a better (in case of high sun) or
753 comparable (in case of low sun) approximation to the flux estimates from the true cloud fields using 3D
754 RT simulations in comparison with those derived from the true cloud fields using 1D RT. Therefore, our
755 conclusion made based on the statistics of all retrievals still holds when failed retrievals are excluded from
756 the analysis. On the other hand, it is also evident that to achieve a better comparison with the flux derived
757 from the true clouds using 3D RT, it is better to include the failed retrievals to preserve the effects of 3D
758 RT.

759 **Appendix B: Surface spectral Albedo plot**
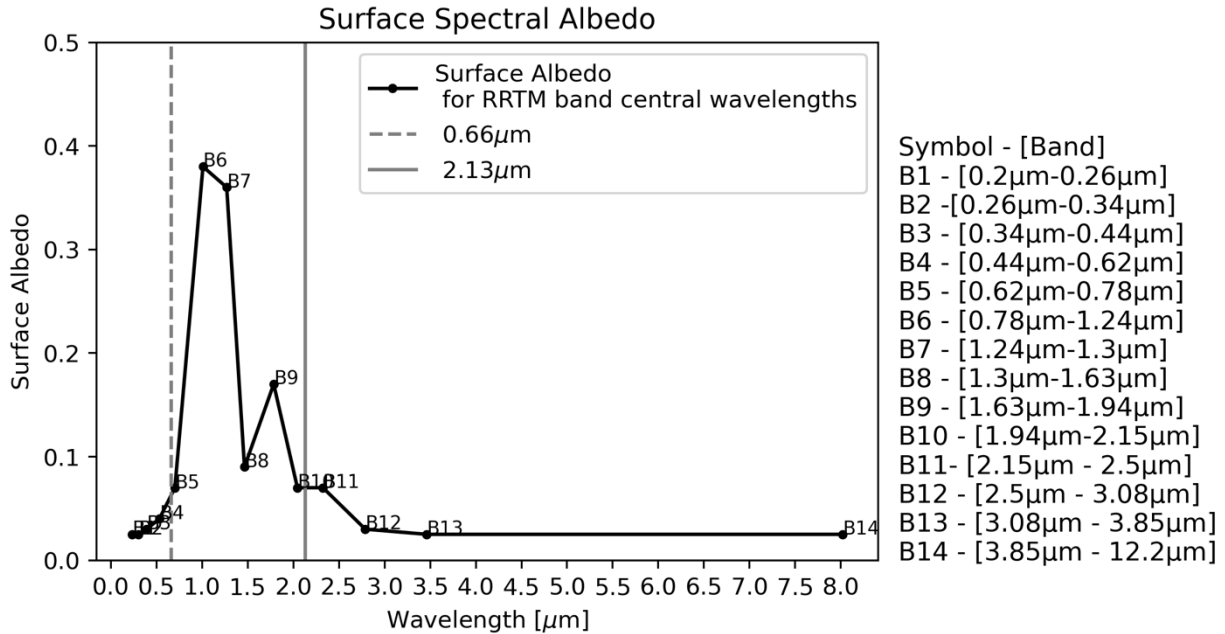
761 Fig.B1. Surface spectral albedo plot utilized in the study. Bi (i ranges from 1 to 14) represent the bands which are in parenthesis.

762 **Author contribution**

763 Conceptualization, Z.Z.; methodology, A.S.A., Z.Z. ; software, A.S.A., Z.Z., ; validation, A.S.A. and Z.Z.;
764 formal analysis, A.S.A.; investigation, A.S.A., and Z.Z.; data curation, A.S.A, Z.Z; writing–original draft
765 preparation, A.S.A.; writing–review and editing, A.S.A.,Z.H.T., J.Z., C.W., S.P., J.W., K.G.M., T.V., Z.Z.;
766 visualization; A.S.A.; supervision, Z.Z.; project administration, Z.Z.; funding acquisition, Z.Z., J.W., K.G.M.,
767 C.W. All authors have read and agreed to the published version of the manuscript.

768 **Competing interest**

769 The contact author has declared that none of the authors has any competing interests.

770 **Acknowledgements**

771 This research has been supported by the NASA ACCESS project (grant no. 80NSSC21M0027). The
772 computations for this study have been performed by the UMBC High Performance Computing Facility
773 (HPCF). The facility is supported by the US National Science Foundation through the MRI program (grant

774 nos. CNS-0821258 and CNS-1228778) and the SCREMS program (grant no. DMS-0821311), with
775 substantial support from UMBC.
776

777 **References**
778

779 Atmospheric Radiation Measurement (ARM) user facility. 2015. LES ARM Symbiotic Simulation and
780   Observation (LASSO) (LASSODIAGRAW108). 2015-06-27 to 2015-06-27, Southern Great Plains
781   (SGP) Central Facility, Lamont, OK (C1). Compiled by W. Gustafson, A. Vogelmann, X. Cheng, S.
782   Endo, B. Krishna, Z. Li, T. Toto, H. Xiao and K. Johnson. ARM Data Center. Data set accessed 2022-
783   11-08 at http://dx.doi.org/10.5439/1342961.
784 Atmospheric Radiation Measurement (ARM) user facility. 2016. LES ARM Symbiotic Simulation and
785   Observation (LASSO) (LASSODIAGRAW113). 2016-08-18 to 2016-08-18, Southern Great Plains
786   (SGP) Central Facility, Lamont, OK (C1). Compiled by W. Gustafson, A. Vogelmann, X. Cheng, S.
787   Endo, B. Krishna, Z. Li, T. Toto, H. Xiao and K. Johnson. ARM Data Center. Data set accessed 2023-
788   05-19 at http://dx.doi.org/10.5439/1342961.
789 Barker, H. W., Jerg, M. P., Wehr, T., Kato, S., Donovan, D. P., and Hogan, R. J.: A 3D cloud-construction
790   algorithm for the EarthCARE satellite mission, Quarterly Journal of the Royal Meteorological
791   Society, 137, 1042-1058, https://doi.org/10.1002/qj.824, 2011.
792 Barker, H. W., Kato, S., and Wehr, T.: Computation of Solar Radiative Fluxes by 1D and 3D Methods Using
793   Cloudy Atmospheres Inferred from A-train Satellite Data, Surveys in Geophysics, 33, 657-676,
794   https://doi.org/10.1007/s10712-011-9164-9, 2012.
795 Cho, H.-M., Zhang, Z., Meyer, K., Lebsock, M., Platnick, S., Ackerman, A. S., Di Girolamo, L., C.-Labonnote,
796   L., Cornet, C., Riedi, J., and Holz, R. E.: Frequency and causes of failed MODIS cloud property
797   retrievals for liquid phase clouds over global oceans, Journal of Geophysical Research:
798   Atmospheres, 120, 4132-4154, https://doi.org/10.1002/2015JD023161, 2015.
799 Coddington, O., Pilewskie, P., Schmidt, K. S., McBride, P. J., and Vukicevic, T.: Characterizing a New
800   Surface-Based Shortwave Cloud Retrieval Technique, Based on Transmitted Radiance for Soil and
801   Vegetated Surface Types, https://doi.org/10.3390/atmos4010048, 2013.
802 Davis, A. B. and Marshak, A.: Multiple Scattering in Clouds: Insights from Three-Dimensional Diffusion/P1
803   Theory, Nuclear Science and Engineering, 137, 251-280, https://doi.org/10.13182/NSE01-A2190,
804   2001.
805 Di Giuseppe, F. and Tompkins, A. M.: Three-dimensional radiative transfer in tropical deep convective
806   clouds, Journal of Geophysical Research: Atmospheres, 108,
807   https://doi.org/10.1029/2003JD003392, 2003.
808 Evans, K. F.: The Spherical Harmonics Discrete Ordinate Method for Three-Dimensional Atmospheric
809   Radiative Transfer, Journal of the Atmospheric Sciences, 55, 429-446,
810   https://doi.org/10.1175/1520-0469(1998)055<0429:TSHDOM>2.0.CO;2, 1998.
811 Gristey, J. J., Feingold, G., Schmidt, K. S., and Chen, H.: Influence of Aerosol Embedded in Shallow Cumulus
812   Cloud Fields on the Surface Solar Irradiance, Journal of Geophysical Research: Atmospheres, 127,
813   e2022JD036822, https://doi.org/10.1029/2022JD036822, 2022.
814 Gristey, J. J., Feingold, G., Glenn, I. B., Schmidt, K. S., and Chen, H.: Surface Solar Irradiance in Continental
815   Shallow Cumulus Fields: Observations and Large-Eddy Simulation, Journal of the Atmospheric
816   Sciences, 77, 1065-1080, https://doi.org/10.1175/JAS-D-19-0261.1, 2020.
817 Gustafson, W. I., Vogelmann, A. M., Li, Z., Cheng, X., Dumas, K. K., Endo, S., Johnson, K. L., Krishna, B.,
818   Fairless, T., and Xiao, H.: The Large-Eddy Simulation (LES) Atmospheric Radiation Measurement
819   (ARM) Symbiotic Simulation and Observation (LASSO) Activity for Continental Shallow
820   Convection, Bulletin of the American Meteorological Society, 101, E462-E479,
821   https://doi.org/10.1175/BAMS-D-19-0065.1, 2020.
822 Hogan, R. J., Fielding, M. D., Barker, H. W., Villefranque, N., and Schäfer, S. A. K.: Entrapment: An

Important Mechanism to Explain the Shortwave 3D Radiative Effect of Clouds, Journal of the Atmospheric Sciences, 76, 2123-2141, https://doi.org/10.1175/JAS-D-18-0366.1, 2019.

Kato, S., Rose, F. G., Sun-Mack, S., Miller, W. F., Chen, Y., Rutan, D. A., Stephens, G. L., Loeb, N. G., Minnis, P., Wielicki, B. A., Winker, D. M., Charlock, T. P., Stackhouse Jr, P. W., Xu, K.-M., and Collins, W. D.: Improvements of top-of-atmosphere and surface irradiance computations with CALIPSO-, CloudSat-, and MODIS-derived cloud and aerosol properties, Journal of Geophysical Research: Atmospheres, 116, https://doi.org/10.1029/2011JD016050, 2011.

Kay, J. E., Hillman, B. R., Klein, S. A., Zhang, Y., Medeiros, B., Pincus, R., Gettelman, A., Eaton, B., Boyle, J., Marchand, R., and Ackerman, T. P.: Exposing Global Cloud Biases in the Community Atmosphere Model (CAM) Using Satellite Observations and Their Corresponding Instrument Simulators, Journal of Climate, 25, 5190-5207, https://doi.org/10.1175/JCLI-D-11-00469.1, 2012.

Kiehl, J. T. and Trenberth, K. E.: Earth's Annual Global Mean Energy Budget, Bulletin of the American Meteorological Society, 78, 197-208, https://doi.org/10.1175/1520-0477(1997)078<0197:EAGMEB>2.0.CO;2, 1997.

Levis, A., Schechner, Y. Y., Aides, A., and Davis, A. B.: Airborne Three-Dimensional Cloud Tomography, 2015 IEEE International Conference on Computer Vision (ICCV), 7-13 Dec. 2015, 3379-3387, 10.1109/ICCV.2015.386,

Liou, K. N.: Radiation and Cloud Processes in the Atmosphere: Theory, Observation, and Modeling, https://doi.org/10.1093/oso/9780195049107.001.0001, 1992.

Loeb, N. G. and Manalo-Smith, N.: Top-of-Atmosphere Direct Radiative Effect of Aerosols over Global Oceans from Merged CERES and MODIS Observations, Journal of Climate, 18, 3506-3526, https://doi.org/10.1175/JCLI3504.1, 2005.

Loveridge, J., Levis, A., Di Girolamo, L., Holodovsky, V., Forster, L., Davis, A. B., and Schechner, Y. Y.: Retrieving 3D distributions of atmospheric particles using Atmospheric Tomography with 3D Radiative Transfer – Part 1: Model description and Jacobian calculation, Atmos. Meas. Tech., 16, 1803-1847, 10.5194/amt-16-1803-2023, 2023.

Marshak, A. and Davis, A. B.: Horizontal Fluxes and Radiative Smoothing, in: 3D Radiative Transfer in Cloudy Atmospheres, edited by: Marshak, A., and Davis, A., Springer Berlin Heidelberg, Berlin, Heidelberg, 543-586, 10.1007/3-540-28519-9_12, 2005.

Marshak, A., Platnick, S., Várnai, T., Wen, G., and Cahalan, R. F.: Impact of three-dimensional radiative effects on satellite retrievals of cloud droplet sizes, Journal of Geophysical Research: Atmospheres, 111, https://doi.org/10.1029/2005JD006686, 2006.

Masuda, R., Iwabuchi, H., Schmidt, K. S., Damiani, A., and Kudo, R.: Retrieval of Cloud Optical Thickness from Sky-View Camera Images using a Deep Convolutional Neural Network based on Three-Dimensional Radiative Transfer, https://doi.org/10.3390/rs11171962, 2019.

Miller, D. J., Zhang, Z., Ackerman, A. S., Platnick, S., and Baum, B. A.: The impact of cloud vertical profile on liquid water path retrieval based on the bispectral method: A theoretical study based on large-eddy simulations of shallow marine boundary layer clouds, Journal of Geophysical Research: Atmospheres, 121, 4122-4141, https://doi.org/10.1002/2015JD024322, 2016.

Miller, D. J., Zhang, Z., Platnick, S., Ackerman, A. S., Werner, F., Cornet, C., and Knobelspiesse, K.: Comparisons of bispectral and polarimetric retrievals of marine boundary layer cloud microphysics: case studies using a LES–satellite retrieval simulator, Atmos. Meas. Tech., 11, 3689-3715, 10.5194/amt-11-3689-2018, 2018.

Mlawer, E. J., Taubman, S. J., Brown, P. D., Iacono, M. J., and Clough, S. A.: Radiative transfer for inhomogeneous atmospheres: RRTM, a validated correlated-k model for the longwave, Journal of Geophysical Research: Atmospheres, 102, 16663-16682, https://doi.org/10.1029/97JD00237, 1997.

Morrison, H. and Gettelman, A.: A new two-moment bulk stratiform cloud microphysics scheme in the Community Atmosphere Model, version 3 (CAM3). Part I: Description and numerical tests,

Journal of Climate, 21, 3642-3659, 2008.

Nakajima, T. and King, M. D.: Determination of the Optical Thickness and Effective Particle Radius of Clouds from Reflected Solar Radiation Measurements. Part I: Theory, Journal of Atmospheric Sciences, 47, 1878-1893, https://doi.org/10.1175/1520-0469(1990)047<1878:DOTOTA>2.0.CO;2, 1990.

Nam, C., Bony, S., Dufresne, J. L., and Chepfer, H.: The 'too few, too bright' tropical low-cloud problem in CMIP5 models, Geophysical Research Letters, 39, https://doi.org/10.1029/2012GL053421, 2012.

Nataraja, V., Schmidt, S., Chen, H., Yamaguchi, T., Kazil, J., Feingold, G., Wolf, K., and Iwabuchi, H.: Segmentation-based multi-pixel cloud optical thickness retrieval using a convolutional neural network, Atmos. Meas. Tech., 15, 5181-5205, https://doi.org/10.5194/amt-15-5181-2022, 2022.

Okamura, R., Iwabuchi, H., and Schmidt, K. S.: Feasibility study of multi-pixel retrieval of optical thickness and droplet effective radius of inhomogeneous clouds using deep learning, Atmos. Meas. Tech., 10, 4747-4759, 10.5194/amt-10-4747-2017, 2017.

Okata, M., Nakajima, T., Suzuki, K., Inoue, T., Nakajima, T. Y., and Okamoto, H.: A study on radiative transfer effects in 3-D cloudy atmosphere using satellite data, Journal of Geophysical Research: Atmospheres, 122, 443-468, https://doi.org/10.1002/2016JD025441, 2017.

Oreopoulos, L., Cho, N., Lee, D., and Kato, S.: Radiative effects of global MODIS cloud regimes, Journal of Geophysical Research: Atmospheres, 121, 2299-2317, https://doi.org/10.1002/2015JD024502, 2016.

O'Hirok, W. and Gautier, C.: A Three-Dimensional Radiative Transfer Model to Investigate the Solar Radiation within a Cloudy Atmosphere. Part I: Spatial Effects, Journal of the Atmospheric Sciences, 55, 2162-2179, https://doi.org/10.1175/1520-0469(1998)055<2162:ATDRTM>2.0.CO;2, 1998.

Pincus, R. and Evans, K. F.: Computational Cost and Accuracy in Calculating Three-Dimensional Radiative Transfer: Results for New Implementations of Monte Carlo and SHDOM, Journal of the Atmospheric Sciences, 66, 3131-3146, https://doi.org/10.1175/2009JAS3137.1, 2009.

Platnick, S., King, M. D., Ackerman, S. A., Menzel, W. P., Baum, B. A., Riedi, J. C., and Frey, R. A.: The MODIS cloud products: algorithms and examples from Terra, IEEE Transactions on Geoscience and Remote Sensing, 41, 459-473, https://doi.org/10.1109/TGRS.2002.808301, 2003.

Platnick, S., Meyer, K. G., King, M. D., Wind, G., Amarasinghe, N., Marchant, B., Arnold, G. T., Zhang, Z., Hubanks, P. A., and Holz, R. E.: The MODIS cloud optical and microphysical products: Collection 6 updates and examples from Terra and Aqua, IEEE Transactions on Geoscience and Remote Sensing, 55, 502-525, 2016.

Rajapakshe, C. and Zhang, Z.: Using polarimetric observations to detect and quantify the three-dimensional radiative transfer effects in passive satellite cloud property retrievals: Theoretical framework and feasibility study, Journal of Quantitative Spectroscopy and Radiative Transfer, 246, 106920, https://doi.org/10.1016/j.jqsrt.2020.106920, 2020.

Ramanathan, V., Cess, R. D., Harrison, E. F., Minnis, P., Barkstrom, B. R., Ahmad, E., and Hartmann, D.: Cloud-Radiative Forcing and Climate: Results from the Earth Radiation Budget Experiment, Science, 243, 57-63, 10.1126/science.243.4887.57, 1989.

Rossow, W. B. and Schiffer, R. A.: Advances in Understanding Clouds from ISCCP, Bulletin of the American Meteorological Society, 80, 2261-2288, https://doi.org/10.1175/1520-0477(1999)080<2261:AIUCFI>2.0.CO;2, 1999.

Singer, C. E., Lopez-Gomez, I., Zhang, X., and Schneider, T.: Top-of-Atmosphere Albedo Bias from Neglecting Three-Dimensional Cloud Radiative Effects, Journal of the Atmospheric Sciences, 78, 4053-4069, https://doi.org/10.1175/JAS-D-21-0032.1, 2021.

Song, H., Zhang, Z., Ma, P.-L., Ghan, S. J., and Wang, M.: An Evaluation of Marine Boundary Layer Cloud Property Simulations in the Community Atmosphere Model Using Satellite Observations: Conventional Subgrid Parameterization versus CLUBB, Journal of Climate, 31, 2299-2320, https://doi.org/10.1175/JCLI-D-17-0277.1, 2018.

Stephens, G. L.: The transfer of radiation through vertically nonuniform stratocumulus water clouds, Radiation in the Atmosphere, 184, 1977.

Stocker, T. F., D. Qin, G.-K. Plattner, M. Tignor, S.K. Allen, J. Boschung, A. Nauels, Y. Xia, V. Bex and P.M. Midgley (eds.: IPCC, 2013: C*limate Change 2013: The Physical Science Basis. Contribution of Working Group I to the Fifth Assessment Report of the Intergovernmental Panel on Climate Change.*, Cambridge University Press, Cambridge, United Kingdom and New York, NY, USA, 1535 pp., 2013.

Tompkins, A. M. and Di Giuseppe, F.: Generalizing Cloud Overlap Treatment to Include Solar Zenith Angle Effects on Cloud Geometry, Journal of the Atmospheric Sciences, 64, 2116-2125, https://doi.org/10.1175/JAS3925.1, 2007.

Trenberth, K. E., Fasullo, J. T., and Kiehl, J.: Earth's Global Energy Budget, Bulletin of the American Meteorological Society, 90, 311-324, https://doi.org/10.1175/2008BAMS2634.1, 2009.

Vardavas, I. and Taylor, F.: Radiation and Climate: Atmospheric energy budget from satellite remote sensing, International Monographs on Ph2011.

Varnai, T., Marshak, A., and Einaudi, F.: Influence of 3D Radiative Effects on Satellite Retrievals of Cloud Properties, 2001.

Várnai, T.: Influence of Three-Dimensional Radiative Effects on the Spatial Distribution of Shortwave Cloud Reflection, Journal of the Atmospheric Sciences, 57, 216-229, https://doi.org/10.1175/1520-0469(2000)057<0216:IOTDRE>2.0.CO;2, 2000.

Várnai, T. and Davies, R.: Effects of Cloud Heterogeneities on Shortwave Radiation: Comparison of Cloud-Top Variability and Internal Heterogeneity, Journal of the Atmospheric Sciences, 56, 4206-4224, https://doi.org/10.1175/1520-0469(1999)056<4206:EOCHOS>2.0.CO;2, 1999.

Várnai, T. and Marshak, A.: Observations of Three-Dimensional Radiative Effects that Influence MODIS Cloud Optical Thickness Retrievals, Journal of the Atmospheric Sciences, 59, 1607-1618, https://doi.org/10.1175/1520-0469(2002)059<1607:OOTDRE>2.0.CO;2, 2002.

Várnai, T. and Marshak, A.: View angle dependence of cloud optical thicknesses retrieved by Moderate Resolution Imaging Spectroradiometer (MODIS), Journal of Geophysical Research: Atmospheres, 112, https://doi.org/10.1029/2005JD006912, 2007.

Welch, R. M. and Wielicki, B. A.: Stratocumulus Cloud Field Reflected Fluxes: The Effect of Cloud Shape, Journal of Atmospheric Sciences, 41, 3085-3103, https://doi.org/10.1175/1520-0469(1984)041<3085:SCFRFT>2.0.CO;2, 1984.

Wielicki, B. A., Barkstrom, B. R., Harrison, E. F., Lee, R. B., Smith, G. L., and Cooper, J. E.: Clouds and the Earth's Radiant Energy System (CERES): An Earth Observing System Experiment, Bulletin of the American Meteorological Society, 77, 853-868, https://doi.org/10.1175/1520-0477(1996)077<0853:CATERE>2.0.CO;2, 1996.

Zelinka, M. D., Klein, S. A., and Hartmann, D. L.: Computing and Partitioning Cloud Feedbacks Using Cloud Property Histograms. Part II: Attribution to Changes in Cloud Amount, Altitude, and Optical Depth, Journal of Climate, 25, 3736-3754, https://doi.org/10.1175/JCLI-D-11-00249.1, 2012.

Zhang, Z. and Platnick, S.: An assessment of differences between cloud effective particle radius retrievals for marine water clouds from three MODIS spectral bands, Journal of Geophysical Research: Atmospheres, 116, https://doi.org/10.1029/2011JD016216, 2011.

Zhang, Z., Ackerman, A. S., Feingold, G., Platnick, S., Pincus, R., and Xue, H.: Effects of cloud horizontal inhomogeneity and drizzle on remote sensing of cloud droplet effective radius: Case studies based on large-eddy simulations, Journal of Geophysical Research: Atmospheres, 117, https://doi.org/10.1029/2012JD017655, 2012.

Zhang, Z., Dong, X., Xi, B., Song, H., Ma, P.-L., Ghan, S. J., Platnick, S., and Minnis, P.: Intercomparisons of marine boundary layer cloud properties from the ARM CAP-MBL campaign and two MODIS cloud

973   products, Journal of Geophysical Research: Atmospheres, 122, 2351-2365,
974   https://doi.org/10.1002/2016JD025763, 2017.
975 Zhang, Z., Werner, F., Cho, H. M., Wind, G., Platnick, S., Ackerman, A. S., Di Girolamo, L., Marshak, A., and
976   Meyer, K.: A framework based on 2-D Taylor expansion for quantifying the impacts of subpixel
977   reflectance variance and covariance on cloud optical thickness and effective radius retrievals
978   based on the bispectral method, Journal of Geophysical Research: Atmospheres, 121, 7007-7025,
979   https://doi.org/10.1002/2016JD024837, 2016.
980 Zhuravleva, T. B., Kabanov, D. M., Sakerin, S. M., and Firsov, K. M.: Simulation of aerosol direct radiative
981   forcing under typical summer conditions of Siberia. Part 1. Method of calculation and choice of
982   input parameters, Atmospheric and Oceanic Optics, 22, 63-73,
983   https://doi.org/10.1134/S1024856009010102, 2009.
984
985
986
987
988